

# Constrained Simulations of the Magnetic Field in the Local Universe and the Propagation of UHECRs

Klaus Dolag<sup>1</sup>, Dario Grasso<sup>2</sup>, Volker Springel<sup>3</sup> and Igor Tkachev<sup>4</sup>

## ABSTRACT

We use simulations of large-scale structure formation to study the build-up of magnetic fields (MFs) in the intergalactic medium. Our basic assumption is that cosmological MFs grow in a magnetohydrodynamical (MHD) amplification process driven by structure formation out of a magnetic seed field present at high redshift. This approach is motivated by previous simulations of the MFs in galaxy clusters which, under the same hypothesis that we adopt here, succeeded in reproducing Faraday rotation measurements (RMs) in clusters of galaxies. Our  $\Lambda$ CDM initial conditions for the dark matter density fluctuations have been statistically constrained by the observed large-scale density field within a sphere of 110 Mpc around the Milky Way, based on the IRAS 1.2-Jy all-sky redshift survey. As a result, the positions and masses of prominent galaxy clusters in our simulation coincide closely with their real counterparts in the Local Universe. We find excellent agreement between RMs of our simulated galaxy clusters and observational data. The improved numerical resolution of our simulations compared to previous work also allows us to study the MF in large-scale filaments, sheets and voids. By tracing the propagation of ultra high energy (UHE) protons in the simulated MF we construct full-sky maps of expected deflection angles of protons with arrival energies  $E = 10^{20}$  eV and  $4 \times 10^{19}$  eV, respectively. Accounting only for the structures within 110 Mpc, we find that strong deflections are only produced if UHE protons cross galaxy clusters. The total area on the sky covered by these structures is however very small. Over still larger distances, multiple crossings of sheets and filaments may give rise to noticeable deflections over a significant fraction of the sky; the exact amount and angular distribution depends on the model adopted for the magnetic seed field. Based on our results we argue that over a large fraction of the sky the deflections are likely to remain smaller than the present experimental angular sensitivity. Therefore, we conclude that forthcoming air shower experiments should be able to locate sources of UHE protons and shed more light on the nature of cosmological MFs.

*Subject headings:* csi — maf — uhc

## 1. Introduction

In spite of decades of experimental and theoretical research on the subject, the nature and origin of Ultra High Energy Cosmic Rays (UHECRs) are still unknown. The experimental study of Ex-

tended Air Showers (EAS) produced by the interaction of UHECRs with the atmosphere provided, so far, only weak constraints on the composition of the primary particles. One of the few established facts is that the primaries of EAS are not standard-model neutrinos, since in this case showers would develop too deep in the atmosphere. Somewhat less certain are the constraints on the allowed fractions of heavy nuclei and photons. The search of a possible asymmetry between vertical and inclined showers made by the Haverah Park collaboration (Ave et al. 2002) allowed the conclu-

<sup>1</sup>Dipartimento di Astronomia, Università di Padova, Padua, Italy

<sup>2</sup>Scuola Normale Superiore and I.N.F.N., Pisa - Italy

<sup>3</sup>Max-Planck-Institut für Astrophysik, Garching, Germany

<sup>4</sup>CERN - Theory Division, Geneva, Switzerland

sion that at energies above  $4 \times 10^{19}$  eV less than 50% of EAS primaries are photons. Concerning the fraction of nuclei, the analysis of the inclined events recorded by the Fly-Eye shower detector (Bird et al. 1993) seems to favor a light composition above  $10^{19}$  eV. Similar results concerning photonic and heavy nuclei fractions were obtained by AGASA (Shinozaki et al. 2003) using muon density in air showers as a primary mass estimator. It is therefore plausible that a significant component of UHECRs is composed of protons or light nuclei.

Besides determining the composition and energy spectrum of UHECR primaries, one of the main goals of EAS experiments is to map the angular distribution of cosmic rays. The angular resolution of these experiments lies generally in the range  $0.5 - 2$  degrees, and may thus in principle allow the identification of UHECR sources with astrophysical counterparts observed in some other channel (optical, radio, X-rays, gamma-rays). While the arrival directions of neutral particles would directly point to the sources (gravitational lensing is negligible), protons and composite nuclei may be deflected by galactic and Extragalactic Magnetic Fields (EGMFs). Note that at extremely high energies,  $E \gtrsim 10^{20}$  eV, UHE protons are not expected to be significantly deflected by the *galactic* magnetic fields. Even at lower energies,  $E \gtrsim 4 \times 10^{19}$  eV, the turbulent component of the MF in the Milky Way does not produce sizable deflections, while the large-scale component gives rise to ordered deflections, such that a reconstruction of the original arrival directions may still be possible (Tinyakov & Tkachev 2002, 2003). However, the very attractive perspective to do charged-particle astronomy with UHECRs might be spoiled by the presence of strong EGMFs.

So far, direct evidence for the presence of EGMFs has been found only in galaxy clusters (see e.g. Carilli & Taylor 2002, a short review of EGMF observations will be also given in section 2.1). The origin of these fields is still unknown. One possibility is that the Intra Cluster Medium (ICM) has been magnetized at low redshift by the ejecta of local sources. If this is the case, EGMFs should be largely confined within galaxy clusters and groups, so that significant deflections of charged UHECRs would have to be expected

only if they cross these structures.

Another possibility is that the seeds of the MFs observed in galaxy clusters have originated at high redshift, before the clusters collapsed and formed gravitationally bound systems. We will discuss possible origins of the intra-cluster magnetic fields in more detail in Section 2.2, and demonstrate in Section 4.2 that this scenario – which is the model studied in our work – leads to cluster MFs which reproduce many observational facts. Note that in this case EGMFs should fill a large fraction of the volume of the universe, so that they might induce considerable deflections of UHECRs traveling over cosmological distances, provided the fields are strong enough. Clearly this is an issue which has to be investigated carefully.

Until recently, the possible effects of EGMFs on the propagation of UHECRs have been investigated by constructing toy models for the structure of the field. Typically, EGMFs were assumed to have a cellular structure, with a Kolmogorov power spectrum at scales smaller than the cell size, and a uniform correlation length and rms field strength. None of these assumptions, however, is well supported by observational or theoretical arguments. Indeed, due to the large conductivity of the IGM, magnetic fields should follow the gas flow and become concentrated and amplified in the high density regions. The assumption of a statistically homogeneous MF is hence not valid in a structured Universe on scales of interest for the problem of UHECR propagation.

In the last few years, several groups started to develop physically more realistic models based on numerical simulations (Ryu et al. 1998; Sigl et al. 2003; Dolag et al. 2003, 2004), combining the magneto-hydrodynamics (MHD) of the magnetized IGM with N-body simulations of the driving gravitational dynamics of the dark matter. Barring this common general approach, the few simulations performed so far differ however not only in their numerical methodology but also in several important aspects of the model assumptions employed, as well as in their final results. The common problem faced by all of these attempts is that one wants to predict the observationally unknown strength and geometry of the magnetic field in low density environments (e.g. filaments and voids) based on a calibration of the underlying model against observations of magnetic

fields in galaxy clusters. This involves an extrapolation over several orders of magnitude in density into a regime where there is no data. Even having such uncertainties, it is nevertheless crucial to demonstrate that the model, in the first place, correctly reproduces available observational data on the cluster scale.

In a recent letter (Dolag et al. 2004), we presented first results of a novel simulation method for the magnetic structure of the Local Universe, where we achieved a number of improvements compared with previous works. First, the initial conditions for the dark matter density fluctuations were constrained to reproduce, to good approximation, the positions and masses of the largest structures (galaxy clusters) observed around the Milky Way. This allows us to remove the ambiguity in the choice of observer position that exists in ordinary simulations, and to obtain the first simulated all-sky maps of expected UHE proton deflections in the magnetic large-scale structure around the Local Group. Since the simulation volume (a sphere with radius  $\sim 110$  Mpc embedded in a box of  $\sim 340$  Mpc on a side) is much larger than considered in previous work, even massive clusters are present in our simulation, allowing for a more accurate comparison with observations. Second, we used a Lagrangian simulation method with an adaptive resolution scheme, which provides for better spatial resolution where it is most needed, namely in the high density regions where the field becomes more tangled. This helps in simulating RMs in galaxy clusters accurately, and hence to establish a reliable baseline for comparing the MHD simulation results with observations. By tracing UHE proton propagation in the simulated magnetic structure obtained in this novel approach, we were then able to show that significant deflections are only expected when galaxy clusters are crossed. Since clusters cover only a very small fraction of the sky, UHECR astronomy should therefore be, in principle, possible.

In this paper, we present a more detailed analysis of the predicted structure of the magnetic field in galaxy clusters, filaments and voids, as well as UHE proton propagation in the simulated magnetic web. Our simulations are very CPU demanding and so far we have made two runs with different initial magnetic seed field. The results of the first run were reported in Dolag et al. (2004). The

analysis of the present paper is mainly based on results obtained in a second simulation, which has been improved in several respects. In this new run, the comoving intensity of the seed field <sup>5</sup> was chosen to be  $B_0 = 2 \times 10^{-12}$  G, a factor 5 smaller than in the previous simulation. This seed field strength leads to a more reasonable match with the magnetic field strengths observed in galaxy clusters, whereas the first simulation was pushing toward the upper limit of field strengths allowed by the data. We changed the orientation of the uniform seed field in order to test a possible dependence of our results on this aspect of the initial conditions. We have also improved the MHD component of our code to account for the back-reaction of the magnetic field on the ionized gas, which in turn may affect the MF in the most dense regions. Our analysis takes into account energy losses of UHE protons on cosmic microwave background (CMB) photons, and we construct deflection maps of protons with an arrival energy of  $4 \times 10^{19}$  eV and  $10^{20}$  eV.

This paper is structured as follows. In Section 2, we give an overview of observations of magnetic fields and the possible origin of magnetic fields in galaxy clusters, which provides the motivation for the model we explore. Section 3 describes the performed simulations, the initial conditions used, and gives a brief description of the simulation code used. Section 4 discusses the predictions of our simulations for the strength and structure of magnetic fields in galaxy clusters and relates these results to observations of Faraday rotation and radio halos of clusters. Section 5 analyses the simulation results for the magnetic field in low density environments like filaments, sheets and voids. In Section 6, we discuss the implications of the simulated magnetic field for the propagation of UHE protons. Finally, we summarize our findings in Section 7. In that section we also compare our approach with that of Sigl et al. (2003,2004a) and discuss the possible reasons of our discrepant results. Throughout this work we assume a background cosmology with  $H_0 = 0.7$ ,  $\Omega_m = 0.3$ ,  $\Omega_\Lambda = 0.7$ , and a baryonic fraction  $\Omega_b/\Omega_m$  of 14%.

---

<sup>5</sup>We define it as a value which the MF seed would have at present if only the cosmological redshift is taken into account. With this definition  $B_0$  does not depend upon initial time.

## 2. Observations of ICMFs and their possible origin

### 2.1. Observations

Direct evidence of the presence of intra-cluster magnetic fields (ICMFs) is provided by observations of extended radio halos in galaxy clusters. Their radiation can only be due to synchrotron emission of relativistic electrons in the ICM. The strength of the ICMFs can be estimated from the intensity of the observed radio emission, either assuming the minimum energy condition, giving  $\langle B \rangle \sim 0.1 - 1 \mu\text{G}$  (Feretti 1999; Giovannini et al. 1993), or by an independent determination of the density of relativistic electrons. The former is frequently used in the literature but it has to be understood as an order of magnitude approach, as there is no compelling physical reason why one should expect the magnetic field to be in equipartition. The latter is made possible for a few clusters by the observation of hard X-ray (HXR) emission that, if interpreted as the outcome of inverse Compton scattering (ICS) of relativistic electrons on CMB photons, implies an average ICMF strength within the emitting volume in the range of  $0.2 - 0.4 \mu\text{G}$  (Fusco-Femiano et al. 1999; Rephaeli et al. 1999). However, both the detection of HXR as well as its interpretation in terms of ICS are still controversial (Rossetti & Molendi 2004; Fusco-Femiano et al. 2004). Other explanations have been proposed which may allow or require stronger ICMF (see e.g. Blasi & Colafrancesco 1999; Atoyan & Volk 1999).

Indeed, Faraday rotation measurements (RMs) of polarized radio sources placed within the cluster, or in the background, provide significant evidence for the presence of stronger ICMFs, in the range  $1 - 10 \mu\text{G}$  in the core of non cooling-flow clusters, and of even larger strength in cooling-flow clusters (Kim et al. 1991; Clarke et al. 2001; Taylor et al. 2001; Vogt & Enßlin 2003, see also Govoni et al., in preparation). Investigations of RMs of elongated radio-sources within galaxy clusters also provide invaluable information on the geometrical structure of ICMFs, which cannot be provided by radio-halo observations alone. The data on RMs are incompatible with uniformly oriented ICMFs, rather, a typical length-scale of  $\approx 5 - 15 \text{ kpc}$  has been inferred. Also, evidence is accumulating that there is no unique length-scale for ICMFs, and

that a successful interpretation of the RMs requires the adoption of a power-law spectrum, even though the power law index (somewhere in the range  $-1.5$  to  $-4$ ) is so far only very weakly constrained (Enßlin & Vogt 2003; Vogt & Enßlin 2003; Murgia et al. 2004). The discrepancy between the EGMF strengths inferred from RMs and those inferred from the combination of radio halos and hard X-ray emission may be explained, at least in part, with the fact that the latter is not sensitive to the presence of magnetic substructures (Enßlin et al. 1999), (for a discussion about this issue and a comprehensive review of EGMF observations see Carilli & Taylor 2002).

Another crucial issue in the present context concerns the radial profile of ICMF in the external regions of galaxy clusters. Recent work based on radio emission (Brunetti et al. 2001) as well as RMs (Dolag et al. 2001) indicates that ICMFs decline in strength with radius, with a radial profile that appears to be similar to that of the gas density.

Outside clusters, only upper limits on the EGMF strength are available. They are at the level of  $10^{-9} - 10^{-8} \text{ G}$  for fields extending over cosmological distances with coherence lengths in the range of  $50$  to  $1 \text{ Mpc}$ , respectively (Blasi et al. 1999). These bounds do not hold for MFs in clustered regions, including the filaments that connect galaxy clusters, where the field strength might be as large as  $10^{-7} \text{ G}$ . In principle, either a weak all pervading smooth field, or stronger fields localized in a complex web of filaments, may produce sizable deflections of UHECR over a large portion of the sky. It is therefore evident that a better understanding of the large-scale magnetic structure of the Universe is called for.

### 2.2. The origin of magnetic fields in galaxy clusters

The origin of the ICMFs is still unknown. We can distinguish three main classes of models that have been proposed to explain their origin.

In the first, EGMFs are assumed to be produced ‘locally’ and at relatively low redshift ( $z \sim 2 - 3$ ) by the ejecta of galaxies (e.g. Völk & Atoyan 2000) or AGNs (e.g. Furlanetto & Loeb 2001). One of the main arguments in favor of these models is that the high metallicity observed

in the ICM suggests that a significant enrichment driven by galactic winds or AGN must have taken place in the past. Winds and jets should carry MFs together with the processed matter. While it was shown that winds from ordinary galaxies give rise to MFs which are far weaker than those observed in galaxy clusters, ICMFs produced by the ejecta of starburst galaxies can be as large as  $0.1 \mu\text{G}$ . Clearly, this class of models predicts that EGMFs are mainly concentrated in galaxy clusters. Note that if the magnetic pollution happens early enough (around  $z \sim 3$ ) these fields will not only be amplified by the adiabatic compression of the proto-cluster region, but also by shear flows, turbulent motions, and merging events during the formation of the galaxy clusters.

In the second class of models, the seeds of EGMFs are assumed to be produced at higher redshift, before galaxy clusters form as gravitationally bound systems. Although the strength of the seed field is expected to be considerably smaller than in the previous scenario, the adiabatic compression of the gas and the shear flows driven by the accretion of structures can give rise to a considerable amplification of the MFs. Several mechanisms have been proposed to explain the origin of magnetic seed fields at high redshift. Some of these models are similar to those discussed above, differing only in the time at which the magnetic pollution is assumed to take place. In the present class of models the MF seeds are supposed to be expelled by an early population of dwarf starburst galaxies or by AGNs at a high redshift between 4 and 6 (Kronberg et al. 1999), allowing them to magnetize a large fraction of the volume. Other models invoke processes which took place in the early universe (see Grasso & Rubinstein 2001, for a review). Indeed, the ubiquity of MFs in the universe suggests that they may have a cosmological origin. In general, all ‘high- $z$  models’ predict MF seeds that fill the entire volume of the Universe. However, the assumed coherence length of the field depends crucially on the details of the models. While models based on phase transitions give rise to coherence lengths which are so small that the corresponding fields have probably been dissipated, MFs generated at neutrino or photon decoupling have much higher chances to survive until the present time. Another (speculative) possibility is that the seed field was produced during inflation. In this case,

the coherence length can be as large as the Hubble radius.

The third scenario is that the seeds of ICMFs were produced by the so-called Biermann battery (Kulsrud et al. 1997; Ryu et al. 1998) effect. The idea here is that merger shocks produced by the hierarchical structure formation process give rise to small thermionic electric currents which, in turn, may generate magnetic fields. The battery process has the attractive feature to be independent of unknown physics at high redshift. Its drawback is that, due to the large conductivity of the IGM, it can give rise to at most very tiny MFs, of order  $10^{-21}$  G. One therefore needs to invoke a subsequent turbulent dynamo to boost the field strength to the observed level. Such turbulent amplification, however, cannot be simulated numerically yet, making it quite difficult to predict how it would proceed in a realistic environment. It is clear that one expects the level of turbulence to be strongly dependent on environment, and that it should mostly appear in high density regions like collapsed objects. While energetic events such as mergers of galaxy clusters can be easily imagined to drive the required levels of turbulence, this is harder to understand in relatively quiet regions like filaments. Lacking a theoretical understanding of the turbulent amplification, it is therefore not straightforward to relate the very weak seed fields produced by the battery process with the magnetic fields observed today. Attempts to construct such models based on combining numerical and analytical computations were not successful so far in reproducing the observed scaling relations of magnetic fields in galaxy clusters.

### 2.3. Simulations of magnetic field evolution in galaxy clusters

As discussed above, a magnetic seed field generated at high redshift is amplified during the formation of galaxy clusters due to the complex dynamics of the gas in which the MF is frozen in. This process has been simulated in previous work (Dolag et al. 1999, 2002) by combining MHD with smoothed particle hydrodynamics (the ‘MSPH’ technique), and with the self-gravity of the gas and an additional collisionless dark matter fluid. It has been shown that MF amplification takes place both due to adiabatic compression and magnetic induction, with the latter being driven by shear

flows that are ultimately powered by anisotropic accretion and merger events.

The fact that the anisotropy of the collapse of galaxy clusters gives rise to additional amplification of magnetic fields has also been demonstrated with analytic models (Bruni et al. 2003). Other simulation work confirmed that merging events of galaxy clusters are a strong driver of magnetic field amplification (Roettiger et al. 1999), and that shear flows play an important role in driving magnetic induction in the ICM (Birk et al. 1999). When applied to the formation of galaxy clusters, these processes produce a magnetic field with a radially varying strength. In the outer region of a cluster, the field is approximately proportional to the density of the gas, while in its core the field profile flattens compared to the density.

One of the main achievements of the MSPH simulations lies in their ability to predict not only the radial magnetic profiles of clusters but also the geometrical structure of the field, which allows the production of synthetic RM maps which can be readily compared with observational data. In doing this, the simulations succeeded in reproducing, or predicting, a number of observational facts. First of all they predicted a nearly linear correlation between X-ray properties and RMs, which was later nicely confirmed by observations (Dolag et al. 2001). This result is of particular relevance here because it shows that the MFs observed in clusters of different masses are well reproduced, and therefore may have plausibly originated in the same cosmological seed field. Applying an additional model for the relativistic electron population within clusters, it was also shown that the basic properties of radio halos, including the very steep observed correlation between cluster temperature and radio halo power, are well reproduced (Dolag & Enßlin 2000). Finally, the predicted radial profiles of RMs fit the observed ones well.

The strength of the uniform seed field required to reach this agreement was  $(1 - 5) \times 10^{-9}$  G at redshift  $z_* \simeq 20$ . In unclustered parts of the intergalactic medium (IGM), this seed field corresponds to  $B_0 \equiv B(z_*)(1+z_*)^{-2} \simeq (0.2-1) \times 10^{-11}$  G at the present time. This range of values is well within the reach of several of the models for magnetic seed field generation that we discussed in the previous section.

It is important to note that due to the chaotic

nature of the cluster accretion process, no memory of the initial field configuration was found in the synthetic ICMFs down to the scales resolved by the simulations. This implies that the results of the simulation depend effectively only on one free parameter, namely the comoving strength of the seed field  $B_0$ . Also, since most of the magnetic field amplification takes place at low redshift ( $z \lesssim 3$ ), the result of the simulation does not depend on the precise time at which the seed field is switched-on, provided it is generated before the first significant major merger events. Within our simulations we found, that at  $z = 3$  the magnetic seed field gets amplified by at most 30% above the expected adiabatic value by the anisotropic collapse within the proto-cluster regions. Therefore, within this scenario it is possible that the seeds of ICMFs were either existing already well before cluster formation, or were generated later, in a local fashion, at  $z \sim 3 - 5$ .

### 3. Constrained MSPH simulation of the Local Universe

#### 3.1. Initial condition for the magnetic field

As we summarized in Section 2.3, the results of MSPH simulations suggest that the MFs observed in galaxy clusters are consistent with originating from a single space-filling cosmological seed field, or from locally generated seeds which have everywhere approximately the same strength. Furthermore, we know that the simulated ICMFs are largely independent of the geometrical structure of the seed field. These facts motivate us to use a homogeneous seed field for our initial conditions.

Following Dolag et al. (1999, 2002), we assume the existence of a cosmological magnetic seed field generated at high redshift. We take the field to be uniform on the scale of the simulation, noting that this will maximize deflections of electrically charged UHECRs. While ICMFs are independent of the adopted seed field orientation, we note that this will not always be true for low density environments on larger scales where some memory of the initial field geometry may survive. Therefore some attention will be required when discussing the generality of our final results.

We performed two simulations with different strengths and orientations of the MF seed. In the first simulation (see Dolag et al. 2004) we

Cluster	$T_{\text{obs}}[\text{keV}]$	$T_{\text{sim}}[\text{keV}]$
Coma	8.2	6.5
Virgo	2.3	3.8
Centaurus	3.5	4.1
Hydra	3.7	3.4
Perseus	5.6	6.2
A3627	7.0	4.0

Table 1: Comparison of the observed cluster temperature with the mass weighted temperature within  $0.1 \times R_{\text{vir}}$  calculated from the simulations.

used  $B_0 = 1.0 \times 10^{-11}$  G, based on earlier work that showed that for this value the magnetic field in galaxy clusters reaches the maximum field strength still allowed by the observations. For the second simulation, we used  $B_0 = 2.0 \times 10^{-12}$  G, which tries to optimize the agreement with the observed RMs rather than maximizing the field strength. The orientation of the seed fields was chosen perpendicular to each other in the two simulations. This allows us to test a possible dependence of our results on the arbitrarily chosen orientation of the seed field.

Note that our two cosmological simulations did not include additional contributions to the magnetic field that are potentially injected into the ICM by galactic winds or AGNs during the late stages of cluster formation. If there is a significant contribution to the cluster magnetic field by such processes, the overall initial cosmological seed field would have to be reduced in order to not exceed the observational bounds. As a further consequence, the magnetic field in low density environments like filaments or voids would then be smaller than predicted by our scenario. Therefore, our predictions for the magnetic field in filaments should be taken as an upper limit.

### 3.2. Initial conditions for the density fluctuations

Our simulations use similar initial conditions as Mathis et al. (2002) in their study of structure formation in the Local Universe. Their initial density fluctuations were constructed from the IRAS 1.2-Jy galaxy survey by first smoothing the observed galaxy density field on a scale of 7 Mpc, evolving it linearly back in time, and then using it as a Gaussian constraint (Hoffman & Ribak 1991)

for an otherwise random realization of the  $\Lambda$ CDM cosmology. The volume that is constrained by the observations covers a sphere of radius  $\sim 115$  Mpc, centered on the Milky Way. This region is sampled with high resolution dark matter particles and is embedded in a periodic box of  $\sim 343$  Mpc on a side. The region outside the constrained volume is filled with low resolution dark matter particles, allowing a good coverage of long range gravitational tidal forces.

Mathis et al. (2002) demonstrated that the evolved state of these initial conditions provides a good match to the large-scale structure observed in the Local Universe. Using semi-analytic models of galaxy formation crafted on top of dark matter merging history trees measured from the simulation, they showed that density and velocity maps obtained from synthetic mock galaxy catalogues compared well with their observed counterparts. Also, many of the most prominent clusters observed locally can be identified directly with halos in the simulation, and their positions and masses agree well with their simulated counterparts.

For the work presented here, we extended the initial conditions by splitting the original high resolution dark matter particles into gas and dark matter particles with masses of  $0.69 \times 10^9 M_{\odot}$  and  $4.4 \times 10^9 M_{\odot}$  respectively. The most massive clusters in our simulations are hence resolved by nearly one million particles. The gravitational force resolution (i.e. the comoving softening length) of the simulations was set to be 10 kpc, which is comparable to the inter-particle separation reached by the SPH particles in the dense centers of our simulated galaxy clusters.

### 3.3. Numerical approach

Our simulations were carried out with GADGET-2, a new version of the parallel TreeSPH simulation code GADGET (Springel et al. 2001). The code uses an entropy-conserving formulation of SPH (Springel & Hernquist 2002), and was supplemented with a treatment of magnetic field in the framework of ideal MHD, as described in Dolag et al. (1999). Besides following the induction equation for the magnetic field, we take magnetic back reaction into account using a symmetric formulation of the Lorentz force based on the Maxwell tensor. The treatment of magnetic fields in SPH was improved by explicitly subtracting the part

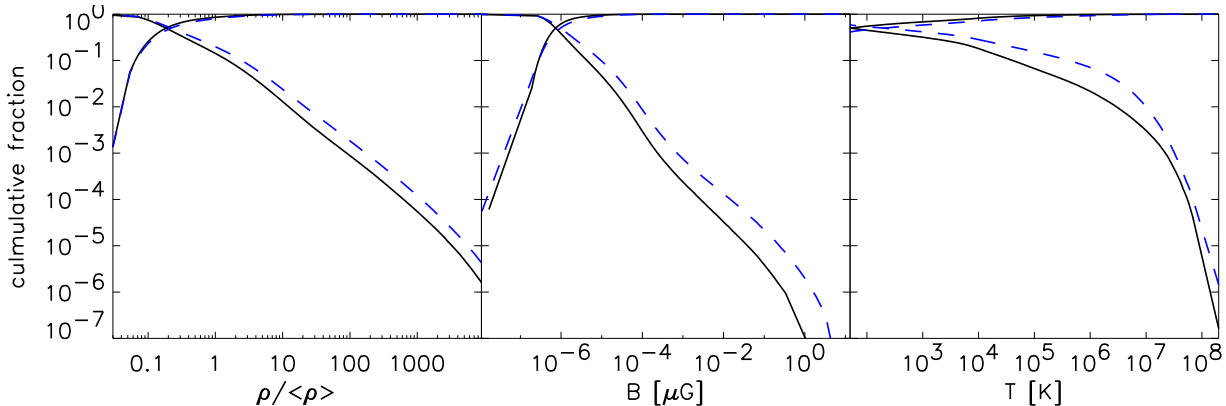


Fig. 1.— Volume-weighted cumulative filling factors of mean baryonic density (left panel), magnetic field strength (middle panel) and gas temperature (right panel). Filling factors are calculated above (decreasing curves) and below (increasing curves) a given threshold, and are shown as a functions of the corresponding thresholds. We present filling factors calculated for two boxes of 70 Mpc on a side, centered on different points in the simulation. The solid lines are for a box centered on the ‘Milky Way’ (observer position), while the dashed lines are for a box centered on a void within the Centaurus supercluster.

of the magnetic force which is proportional to the divergence of the magnetic field, as described in Børve et al. (2001). This helps to keep the level of any numerically induced divergence of the magnetic field at negligible values, and it also helps to avoid a well-known instability of our MHD formulation in regions where magnetic field pressure substantially exceeds the thermal pressure.

Note that in simulations without radiative cooling, like the ones we carry out here, the magnetic field pressure stays well below the thermal one, even within the cores of the most massive galaxy clusters. In very strong shocks, it can however still happen that the magnetic field is compressed so substantially that magnetic forces dominate the thermal ones for brief periods of time. Such situations are handled more accurately with our new formulation. In particular, test simulations with magnetic shock tubes showed that the use of the entropy-conserving formulation of SPH noticeably reduces the noise level in the solution of the MHD equations.

## 4. Results

### 4.1. General properties of the simulation

As in Mathis et al. (2002), we find that dark matter halos identified in our simulations match real observed galaxy clusters in the Local Universe

well in their masses and positions. Since our simulations now also include the cosmic gas, we can extend this comparison to properties of the intra-cluster medium (ICM). In Table 1, we compare the ICM temperature of local clusters (derived from X-ray observations) with the temperatures of the corresponding objects in our hydro simulation. While the agreement is not perfect, it can still be considered to be quite good, given in particular that the details of the hydrodynamics involved in the cluster formation process are not directly restricted by the constraints imposed by the IRAS 1.2-Jy survey. Reassuringly, the comparison hence suggests that the large-scale structure in the hydrodynamic component of our simulation can serve as a good model for the real structure within the Local Universe.

In Figure 1, we show the cumulative volume-weighted distribution functions of baryonic density, magnetic field strength, and gas temperature for a  $(70 \text{ Mpc})^3$  box extracted around the ‘Milky Way’ (our observer position). Except for the cluster cores (highest densities), it is evident that the distributions of density and magnetic field are very similar, even at low densities outside of galaxy clusters. For comparison, we also show measurements for an equally sized box, but centered on a relative void within the Centaurus super-cluster. In this environment, the filling factors inferred



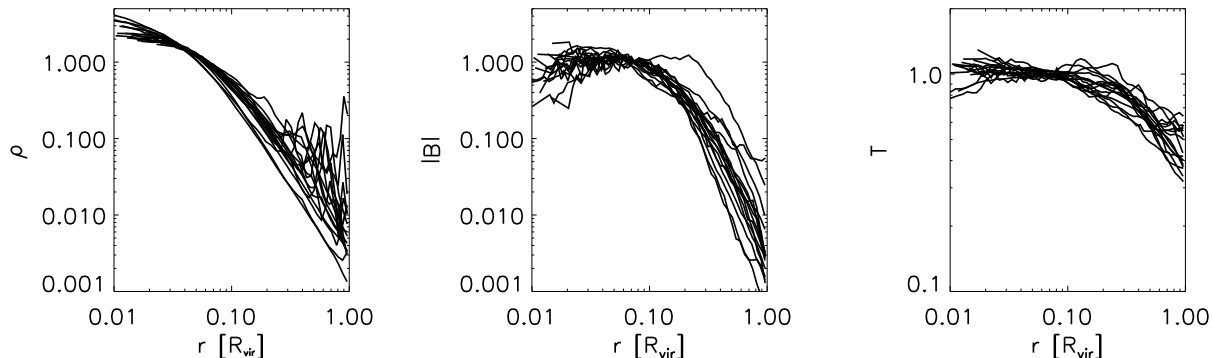


Fig. 2.— Spherically averaged profiles of gas density (left panel), magnetic field strength (middle panel) and temperature (right panel, mass-weighted) for the 16 most massive clusters extracted from the simulation. The profiles are scaled to  $R_{\text{vir}}$  and normalized to have the same mean value within  $0.1 \times R_{\text{vir}}$ .

for the same threshold in density (or magnetic field strength) are roughly one order of magnitude larger. Note that for both positions, the nearest galaxy clusters are located at a distance of  $\sim 20$  Mpc. This demonstrates the importance of choosing a realistic observer position within a comparable environment if one wants to quantitatively assess the effects of the EGMF around the Milky Way.

#### 4.2. Predicted MF scalings in galaxy clusters

As we discussed in Section 2.1, galaxy clusters are the only structures where EGMFs are actually observed. To verify the consistency of our simulated model it is therefore important to investigate its predictions for cluster magnetic fields and to contrast them with observational data.

We begin by considering radial profiles of the gas density, temperature, and magnetic field in galaxy clusters formed in our simulation. In Figure 2, we show the mass-weighted averages of these quantities computed for gas particles contained in spherical shells centered on the halo centroids. The median density profile is compatible with the canonical  $\beta$ -model,

$$n_{\text{gas}}(r) = n(r_c) \left(1 - \frac{r^2}{r_c^2}\right)^{-3\beta/2}, \quad (1)$$

for  $r > r_c \simeq 250$  kpc. Consistent with earlier results (Dolag et al. 2002), we find that the magnetic field profiles follow, on average, the density

profiles of clusters in their outer parts, whereas in the central regions the magnetic field profiles flatten. This flattening is presumably a direct consequence of the lower gas velocities in the cluster cores, which make magnetic induction less effective.

Depending on the cluster and its dynamical state, the slope of the magnetic profile in the outer parts scatters somewhat around the slope of the gas density. Also, the size of the magnetic core shows substantial system to system variation. On average, however,  $B$  is to first order proportional to  $n_{\text{gas}}$ . As mentioned in Section 2.1, such a scaling can be tested by comparing predicted and observed correlations between the X-ray surface brightness and the RMs.

The amplification of the magnetic field within our simulations is not only due to the adiabatic compression of the gas but also due to magnetic induction driven by shear flows. If induction is important, we expect that the final magnetic field in galaxy clusters will depend on their merging history. In particular, more massive clusters, which undergo more numerous and more energetic merger events, should end up with a higher final magnetic field in their cores than less massive ones. On the other hand, pure adiabatic compression should not lead to a significant dependence of the central magnetic field on cluster mass or cluster temperature, because the central gas density within galaxy clusters does not depend strongly on the mass of the system.

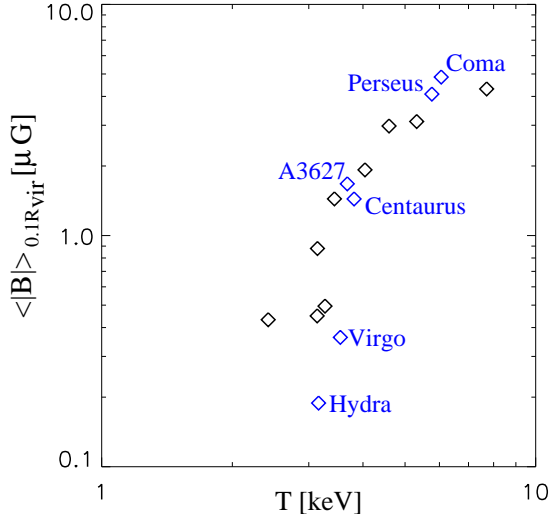


Fig. 3.— Magnetic field strength vs. temperature for the most massive clusters of the simulation. We have labeled those halos that are identified with actual clusters. The magnetic field has been mass-averaged within  $0.1 \times R_{\text{vir}}$ , resulting in mean values representative for the cluster cores.

Figure 3 shows the mass-averaged magnetic field calculated within  $0.1 \times R_{\text{vir}}$  as a function of the gas temperature in the cores of the most massive clusters found in the simulation. It is evident from this figure that the simulation predicts a strong dependence of  $\langle B \rangle$  on temperature, showing that the build-up of the magnetic field is dominated by induction and not compression. Note that the slope of the  $\langle B \rangle$ - $T$  correlation predicted by our simulation is comparable with that found in earlier work (Dolag et al. 2002), but the normalization is higher. This is not unexpected, as in the present study the numerical mass-resolution is 20 times better, such that the magnetic field can be tangled on much smaller scales. In this case the value of  $\langle |\vec{B}| \rangle$  can be larger, without increasing the predicted RM values.

The power spectrum of the magnetic field in the largest clusters of this simulation has been determined by Rordorf et al. (2004) finding that, on average, it is slightly steeper than a Kolmogorov spectrum. Significant scatter has been found about this mean behavior, which may depend on the cluster merger history. We remark

that the resolution limit of our simulations is already close to (to within a factor of two), but still slightly larger than, the smallest length scales inferred for the magnetic field based on high resolution mapping of elongated radio sources within galaxy clusters.

### 4.3. Comparison with observations

Our improved numerical resolution allows us to take the tangled structure of ICMFs and its consequences for RMs much better into account than was possible in previous work. It is therefore interesting to repeat and extend previous comparisons of MSPH simulations with observational data (Dolag et al. 2001, 2002; Dolag & Enßlin 2000). For the first time we are also able to study clusters extracted in a volume-limited fashion from a cosmological simulation, instead of having to work with a sample of cluster re-simulations with a poorly defined selection function. Thanks to the constrained nature of our simulation, we can also use the simulated ‘Coma’ cluster directly as a reference and calibration point. In the following, we therefore consider in some detail a comparison with data on RMs, X-ray correlations, and radio halos, respectively.

#### 4.3.1. Rotation measure profiles

In Figure 4, we compare simulated RMs with observational data constructed from two independent samples of rotation measurements of point-like sources in or behind of Abell clusters (taken from Kim et al. 1991; Clarke et al. 2001). We plot the absolute value of the RM as a function of distance from the centroid of the closest Abell cluster. The solid line gives the median of the distributions in each of the 15 bins we used for binning the data.

Note that due to the construction of these samples, the underlying selection function for the contributing galaxy clusters is ill-defined. This is of importance, as the RM signal depends on cluster mass. One therefore expects a dependence of the median profile on the mass function of the selected clusters. As the cluster sample is composed out of Abell clusters, it is however reasonable to assume that it mainly consists out of comparatively massive galaxy clusters.

We also included in the plot the values inferred from three elongated sources (diamonds) observed

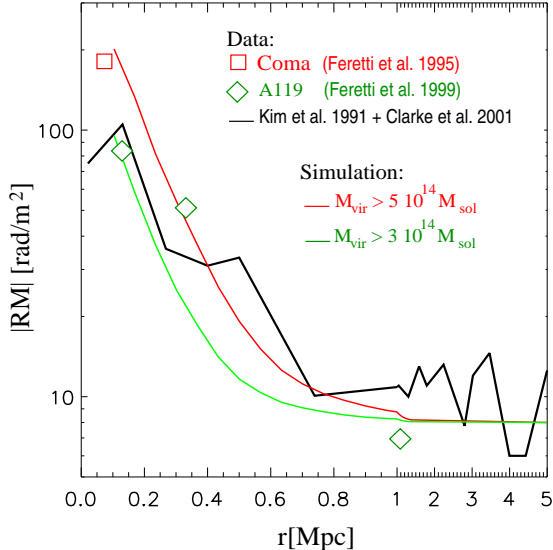


Fig. 4.— Comparison of RMs from the simulation with observations for Abell clusters, as a function of distance to the closest cluster. Smooth lines represent median values of  $|\text{RM}|$  produced by simulated clusters with masses above  $5 \times 10^{14} M_{\odot}$  and  $3 \times 10^{14} M_{\odot}$ . The broken line represents the median of combined data taken from the independent samples in Kim et al. (1991) and Clarke et al. (2001). We also include data (diamonds) for the three elongated sources observed in A119 (Feretti et al. 1999a), and for the elongated source observed in the Coma cluster (Feretti et al. 1995).

in the single galaxy cluster A119 (Feretti et al. 1999a). This cluster compares well with the median profile. Having a temperature of  $\simeq 5.6$  keV it also indicates that the RM profile extracted from the observations reflects the profiles of massive galaxy clusters. We also added one data point from the elongated source observed in the Coma cluster (Feretti et al. 1995). Coma has a slightly higher temperature ( $\approx 8.2$  keV) but fits well into the global trend for massive clusters.

We calculated synthetic RM maps of the most massive clusters performing line of sight integrations of

$$\text{RM} = 812 \frac{\text{rad}}{\text{m}^2} \int \frac{n_e}{\text{cm}^{-3}} \frac{B_{\parallel}}{\mu\text{G}} \frac{dl}{\text{kpc}}, \quad (2)$$

where  $B_{\parallel}$  is the magnetic field component along the line of sight and  $n_e$  is the electron density

which is found assuming complete ionization and primordial H/He composition.

For comparison of the observed profile with the expectations based on synthetic RM maps obtained from our simulations we have considered two different lower mass cuts for selecting the simulated clusters,  $5 \times 10^{14} M_{\odot}$  and  $3 \times 10^{14} M_{\odot}$ , respectively. Clearly, as smaller clusters are more numerous and give rise to smaller RMs, the prediction of the simulation will depend on the adopted mass cut. Figure 4 shows that our simulation reproduces the combined radial profiles of the RMs quite well, as well as that for the individual cluster A119, using a reasonable mass-cut within the range  $3 - 5 \times 10^{14} M_{\odot}$ . Note that the observations do not drop to zero for large impact parameters. Based on the averaged value on scales between 1 and 3 Mpc we added a value of  $8 \text{ rad/m}^2$  to the synthetic measurements to approximately mimic the errors and noise of the measurements.

#### 4.3.2. Scaling with X-ray measurements

Another powerful test is obtained by studying the correlation between X-ray flux and rotation measure, at the position of the radio galaxy where the rotation measure is observed. This amounts to comparing two line-of-sight integrals: Eq. (2) for RM with

$$\int n_e^2 \sqrt{T} dl, \quad (3)$$

the latter being proportional to the X-ray flux. Since the  $\sqrt{T}$  dependence can be safely neglected here, this allows us to measure how (on average) the magnetic field scales with density. Furthermore, as we compare the same line-of-sight for both measures, this test is independent of model assumptions for the density distribution, or a possible asymmetry of the galaxy cluster.

We have measured this correlation from synthetic observations of our clusters, and fitted the results obtained for individual clusters by power laws. We find the slopes  $\alpha$  to vary between 0.8 and 1.1, in agreement with previous results (Dolag et al. 2001). On the other hand, from the assumptions that the gas density  $n_{\text{gas}}$  in the cluster follows a  $\beta$ -profile, Eq. (1), and that the magnetic field strength is scaling with the gas density as

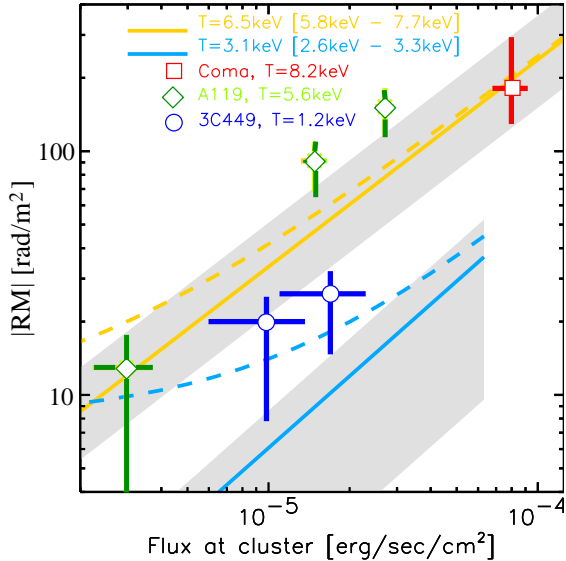


Fig. 5.— Correlation of rotation measurements with X-ray surface brightness for different galaxy clusters. The data points are observations for the two massive clusters A119 (Feretti et al. 1999a) and Coma (Feretti et al. 1995), and for the very poor ( $T \approx 2$  keV) system 3C449, which has a central radio source (Feretti et al. 1999b). The predictions from the simulations are obtained by averaging over the 5 most massive clusters (upper gray region), or all clusters in the range 2.5 – 3.5 keV (lower gray region). The dashed line represents the predictions from the simulations, if we account for errors and noise within the real observations by adding 8 rad/m<sup>2</sup>.

$B \propto (n_{gas})^\gamma$ , it follows (Dolag et al. 2001)

$$\alpha = 0.5 \frac{3\beta(1 + \gamma) - 0.5}{3\beta - 0.5}. \quad (4)$$

For the usual value of  $\beta = 0.75$  and a magnetic field proportional to  $n_e$  (i.e.  $\gamma = 1$ ) this leads to  $\alpha \approx 1.1$ .

Figure 5 compares the observed relation between surface brightness and rotation measure with the results of our simulations. We consider two sub-samples of simulated clusters, one containing the 5 most massive ones, and the other consisting of relatively low-mass systems. The high mass clusters span the range 6.6 – 8.2 keV in temperature (upper band), whereas the lower mass systems span the range 2.8 – 3.5 keV (lower

band). The region shaded in Gray marks the range of correlations we found within these subsets, and the lines give the average correlations in the two cases. We included observational data points for two massive clusters, A119 (Feretti et al. 1999a) and Coma (Feretti et al. 1995), as well as for a very poor system ( $T \approx 2$  keV) hosting the central radio source 3C449 (Feretti et al. 1999b). Note that the data points for A119 and Coma appear somewhat differently in Figs. 4 and 5. This arises because for both elongated sources for uniformity with other data in the first plot we calculate the median of the RM across the source area, while in the second plot we calculate the rms of the rotation measure.

Our magnetic field strength, which was chosen to give the best agreement with the radial profile for RMs, lies at the lower bound of the observations in this comparison. However, the slope of the correlation is well reproduced, and also the trend with temperature we find in the simulations seems to be confirmed by the observations. More data, especially for higher cluster temperatures, will be needed to draw definite conclusions though, particularly since this comparison has the potential to be affected by a number of systematic effects. As the synthetic RMs are drawn from ideal observations, they are free of noise and measurement errors, which could however be significant for small observed RM values. To illustrate this, we have added a dashed line for the synthetic observations, representing the predictions from the simulations if errors or noise within the real observations are roughly modeled by adding 8 rad/m<sup>2</sup> to the synthetic observations. Given that the properties of the noise and the nature of systematic errors of the observations are hard to quantify, this should be only taken as a fiducial estimate of the potential influence of plausible measurement errors.

Note that the X-ray observations, but also the predictions of X-ray fluxes obtained from the simulations, are subject to systematic effects as well. For example, it is well known that adiabatic simulations, as used in this study, tend to overproduce the X-ray emission of galaxy clusters compared with simulations which also account for effects of radiative cooling and stellar feedback. Interestingly, if we reduce the emission inferred from the simulations by a factor of 2 to roughly account for this, a better agreement between simulations and observations is achieved.

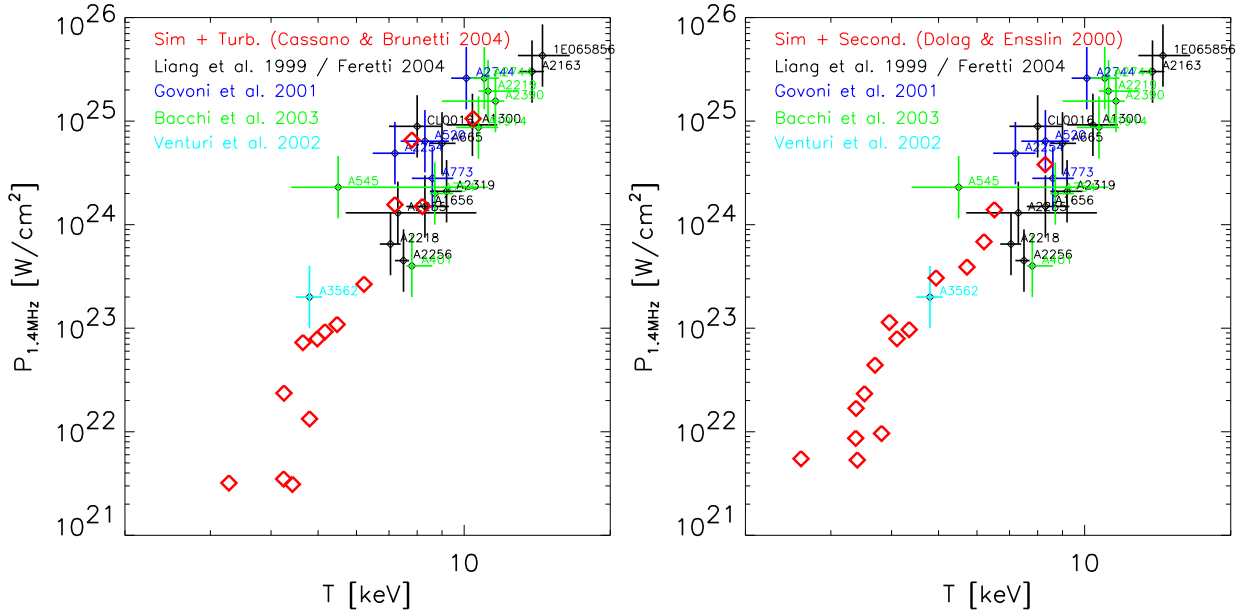


Fig. 6.— Total power of radio halos observed at 1.4 MHz vs. cluster temperature. We plot data from Liang et al. (2000), which were partially re-observed by Feretti (2004, in preparation) together with data from Govoni et al. (2001); Bacchi et al. (2003); Venturi et al. (2003). To compare with our simulations, we applied two different models for the relativistic electron component in galaxy clusters. In the panel on the left, we show the result obtained from a primary model based on acceleration by turbulence (Cassano & Brunetti 2004, in prep.), while for the panel on the right, we used a secondary hadronic model as described in Dolag & Enßlin (2000). Both models were normalized so that our simulated Coma cluster has the same radio luminosity as observed for the real Coma cluster. The slope of the observational data is reproduced well by our simulated clusters in both cases.

#### 4.3.3. Radio Halos

The scaling relations of magnetic fields in clusters are also expected to leave an imprint in observations of radio halos. Note that it is still unclear how the relativistic electron component in galaxy clusters is accelerated and maintained over the cluster volume. The various models can be grouped into two classes: primary models, where the relativistic electrons are directly (re-)accelerated by various mechanism (shocks, turbulence etc.) and secondary models, where a population of relativistic protons is accelerated which then, by hadronic interactions with the ICM, can produce or maintain a population of relativistic electrons (for an overview of models, see Sarazin 2002; Enßlin 2002; Brunetti 2003). Independent of the model for the production of the relativistic electrons and its dependence on the cluster temperature, the resulting emitted radio power car-

ries always an additional dependence on  $B^2$ , so that any strong relation between magnetic field and cluster temperature will have a significant imprint on the scaling of radio power with cluster temperature.

In recent work, Cassano & Brunetti (2004, in preparation) developed a semi-analytic model where they related the turbulence injected by major cluster mergers with the acceleration of relativistic electrons. For this model, the expected radio luminosity produced during a major merger roughly scales as

$$P \propto \frac{M_{\text{vir}}^3}{\sqrt{T_{\text{vir}}}} \frac{B_{\text{core}}^2}{B_{\text{CMB}}^2 + B_{\text{core}}^2}, \quad (5)$$

where we, as usual, express the electron Compton energy losses on the CMB in terms of equivalent effective magnetic field strength,  $B_{\text{CMB}} = 3.24 \mu\text{G}$ . Assuming this scaling, we can produce a predicted correlation between radio power and cluster tem-

perature based on values inferred from our simulated clusters. Figure 6, left panel, shows a comparison of a collection of observations with the prediction obtained from our cluster set using the model Eq. (5). We normalized the relation using Coma as a calibration point. For the right panel, we used a secondary model as described in Dolag & Enßlin (2000), again calibrating the zero point of the relation with the Coma cluster. Note that in this second case, the model is applied on a particle by particle basis when calculating the radio emissivity by integrating over the whole cluster volume. Both scenarios are in good agreement with the observations, supporting the validity of our simulations as a reasonable model for the magnetic field in real galaxy clusters, but we cannot discriminate between different models for the origin of the radio plasma at this point. Interestingly, the secondary model shows noticeably less scatter, which might be a consequence of its local definition, which more directly accounts for the cluster geometry.

## 5. The large-scale structure of cosmic magnetic fields

Galaxy surveys show that clusters appear to be linked with each other by a network of feeble *filaments*. These patterns in the galaxy distribution are successfully reproduced by N-body simulations of CDM models, which have established the existence of a ‘cosmic web’, consisting of sheets and filaments of matter around large underdense voids. In the hierarchical structure formation process, dark matter and gas accrete onto the filaments and then flow along them towards large groups and clusters, the nodes of the cosmic web. As the gas collapses onto filaments, we hence expect not only adiabatic compression, but also shear flows along the filament axis, which may amplify a pre-existing MF significantly. In voids on the other hand, where galaxies are almost absent and where the dark matter and gas densities are expected to be significantly smaller than their cosmological mean values, we expect that a pre-existing MF will only be diluted by the cosmic expansion. No direct measurements of MFs in either filaments or voids are available; this makes it particularly interesting to explore the predictions of our simulation for the magnetic field configuration within these large-scale structures.

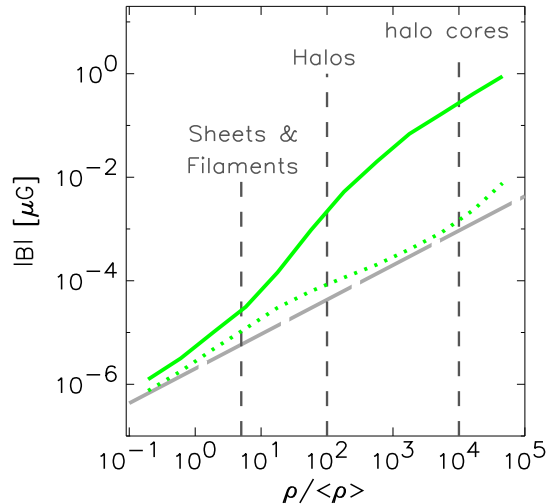


Fig. 7.— The magnetic field strength as a function of baryonic overdensity. The long dashed line shows the expectation for a purely adiabatic evolution, the solid line gives the mean field strength at a given overdensity in our simulation. While the latter is close to the adiabatic value in underdense regions, there is a significant inductive amplification in clusters due to shear flows and turbulence, subject however to saturation in the cluster cores. At any given density, a large fraction of particles remains close to the adiabatic expectation, as shown by the dotted line, which gives the median of the distribution at each density.

Before we consider filaments and voids in more detail, we consider in Figure 7 a global view of the field strength as a function of baryonic overdensity. As expected, the field stays close to adiabatic evolution in underdense regions, but already for mildly overdense structures like sheets and filaments, a significant amplification above the value for adiabatic compression can be observed. This inductive amplification of the mean magnetic field becomes stronger towards the high densities reached in the cores of clusters, where it saturates.

### 5.1. Magnetic fields in filaments and sheets

In the following, we focus on the Centaurus supercluster region, which gives rise to one of the most prominent features within synthetic deflection maps for UHECRs traversing the Local Uni-



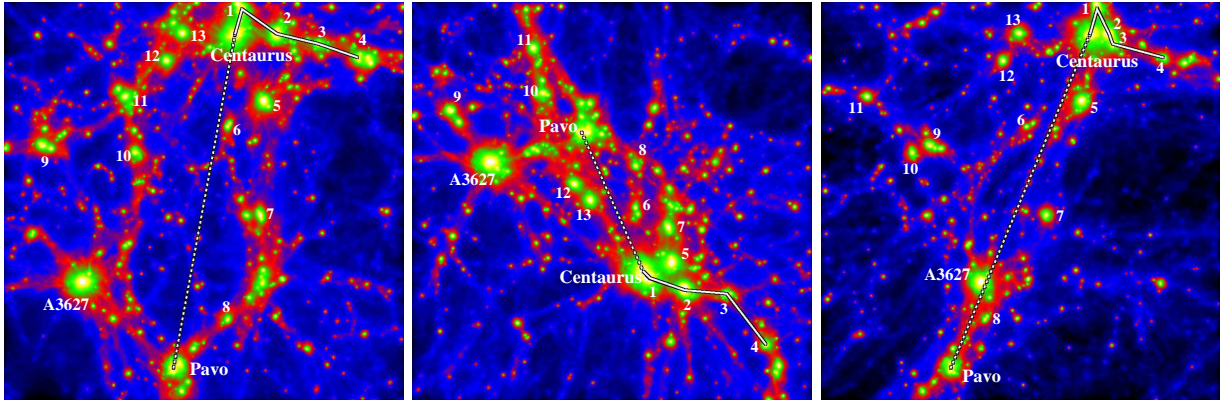


Fig. 8.— Maps of the projected gas density for a region centered on a large structure around Centaurus, Pavo and A3627. The extent of the region is 50 Mpc. Positions of several other massive halos are labeled to underline the 3D geometry. The solid and the dotted lines mark the path along which we show the physical state of the gas in Figures 9 and 11 respectively.

verse (see our results in Section 6). Figure 8 shows three projections of the gas density of this region obtained from a  $(50 \text{ Mpc})^3$  cube extracted from the simulation. Despite containing a huge void, which can be seen in the left panel, the whole region still represents a large over-density. In fact, the average density within the region is nearly an order of magnitude larger than the average density of an equally sized volume centered on the position of the Milky Way (see also Fig. 1).

Comparatively little is known about the details of the physical state of the baryonic gas within filaments. An important reason for this lies in their low density, which strongly limits the resolution achieved by cosmological simulations for the dark matter component of filaments. Note that since the dark matter is the dominant mass component that drives via its gravity the formation and evolution of filaments, any hydrodynamic simulation is ultimately restricted in its resolution to that of the dark matter component. Also, filaments are not relaxed and usually have a quite complex geometric structure, far from being simple straight connections between clusters. Instead, they are often projections or crossings of sheet-like structures that form the envelope around underdense voids. Figure 8 demonstrates this nicely. For example, in the left panel, there appear to be two prominent filaments which connect the *Pavo* cluster with the *Centaurus* cluster (the left one of the two filaments

includes the cluster *A3627*). However, looking at different projections of the same region (center and right panels), the situation turns out to be more complex; what appeared as two filaments is really the projection of a complex group consisting of several dozen halos. We have marked the 16 most massive halos within the region to show the underlying three-dimensional structure.

In Figure 9, we show the gas density, temperature, magnetic field strength and orientation, along a filamentary structure connecting a chain of 5 halos which build an almost linear, 23 Mpc long structure joining into the halo identified with the *Centaurus* cluster (see the solid line in Fig. 8 for the actual path). This line passes through a high concentration of clusters on a relatively short distance. Note that for the first bridge ( $\approx 3.3$  Mpc long), the two virial radii overlap, so that this part is characterized best as a high density bridge between the first two halos. Here the lowest density within the bridge corresponds to an overdensity  $\delta$  close to 200, whereas between the last two halos, which are roughly 9 Mpc apart, the density of the filament drops to  $\delta \sim 40$ . The temperature profile along the filament is smoother and less steep compared with the density, ranging from  $10^8$  K in the halo identified with the *Centaurus* cluster to  $10^6$  K in the most tenuous regions of the filament. Note however the numerous jumps in the temperature, in particular in the last part of the filament,

indicating the presence of several strong shocks running along it.

To give an idea of the spatial resolution achieved within these structures, we also plot the mean inter-particle separation of gas particles along the filament. Given that the gas follows the dark matter well and that we have chosen an equal number of gas and dark matter particles, this is also a good measure of the mean inter-particle separation of the underlying dark matter distribution. As we stressed earlier, the maximum resolution within filaments is restricted by the mass and spatial resolution of the underlying dark matter N-body simulation ( $4.4 \times 10^9 M_\odot$  in our case), independent of the spatial resolution of the hydro scheme used.

When considering the absolute value of the magnetic field along the selected line through the 5 halos, we see that the fluctuations in field strength lie between  $10^{-2}$  and  $10^{-3} \mu\text{G}$  in the high density bridge between the first two clusters, while they go down to around  $10^{-4} \mu\text{G}$  in the regions with the lowest density contrast. We can also see that the magnetic field strength in the low mass system is much smaller than in the high mass systems, as expected based on the strong relation we found between mean magnetic field in cluster centers and cluster temperature. Note in this respect that the central density within the small mass system is close to the value found in the high mass systems. This shows that the magnetic field amplification has involved not only adiabatic compression but must have been driven also by strong shear flows and merger events, which were more effective in the larger clusters.

The regions shaded in gray mark places where the angle between the magnetic field and the path marked in Fig. 8 is less than 45 degrees. Often large-scale flows twist the field but the field strength is largely unchanged. MF rotations are most intense in clusters, where the gas flows are in general very dynamic. At the positions of shocks, the changes in the field direction can be very sharp, even in low density regions. In the high-density segment of the filament between the two close massive clusters, the MF is chaotically oriented, suggesting that it keeps no memory of the seed field structure. On the other hand, in the peripheral segment where the density stays quite low and non-linear effects are weak, the field is co-

herently oriented, and reflects the structure of the initial seed field. In this low-density environment, essentially only adiabatic compression is operating. Note that the  $\rho^{(2/3)}$  expectation for adiabatic amplification assumes an isotropic collapse, which is not really true for filaments, where particularly low-density filaments maintain a memory of the direction of the seed field. For a given filament, we therefore expect a dependence of the field amplification on the direction of the seed field. However, because a cosmological simulation contains filaments of all directions, statistical inferences like the average magnetic field strength within filaments should be unaffected by this dependence.

We now turn to examining the structure of the magnetic field orthogonal to filaments. To this end, we consider a plane located in the middle between the last two halos, orthogonal to the filament studied above. The panels in the left column of Figure 10 show contours of density and temperature out to a distance of 10 Mpc from the filament. As can be seen from the density map, the filament connects several sheets that extend from it in a radial fashion. Interestingly, in the temperature map, only the massive sheets are visible and the filament itself looks noticeably rounder and larger in extent. The middle and right panel on top show the absolute value of the magnetic field for the two simulations we performed. Apart from the offset in amplitude, which is a direct consequence of the different strengths of the initial seed fields, the structure obtained from the two simulations looks remarkably similar and corresponds to the structure observed in the density very well.

The two bottom panels on the right of Figure 10 show the orientations of the two magnetic field vector components within the plane, normalized using all three components. The different orientations of the magnetic field vectors in the two cases are a result of the different orientation of the initial magnetic seed field in the two simulations. While the distortion pattern of the field is not exactly the same in the two cases, large similarities are nevertheless present. The field is never really highly chaotic in the low density filament that crosses the plane in the center, but it is clearly more tangled in the filament core, and along the densest sheet, which testifies to the presence of shear flows in these structures. In the low density parts away from the filament, the MF keeps its coherent struc-



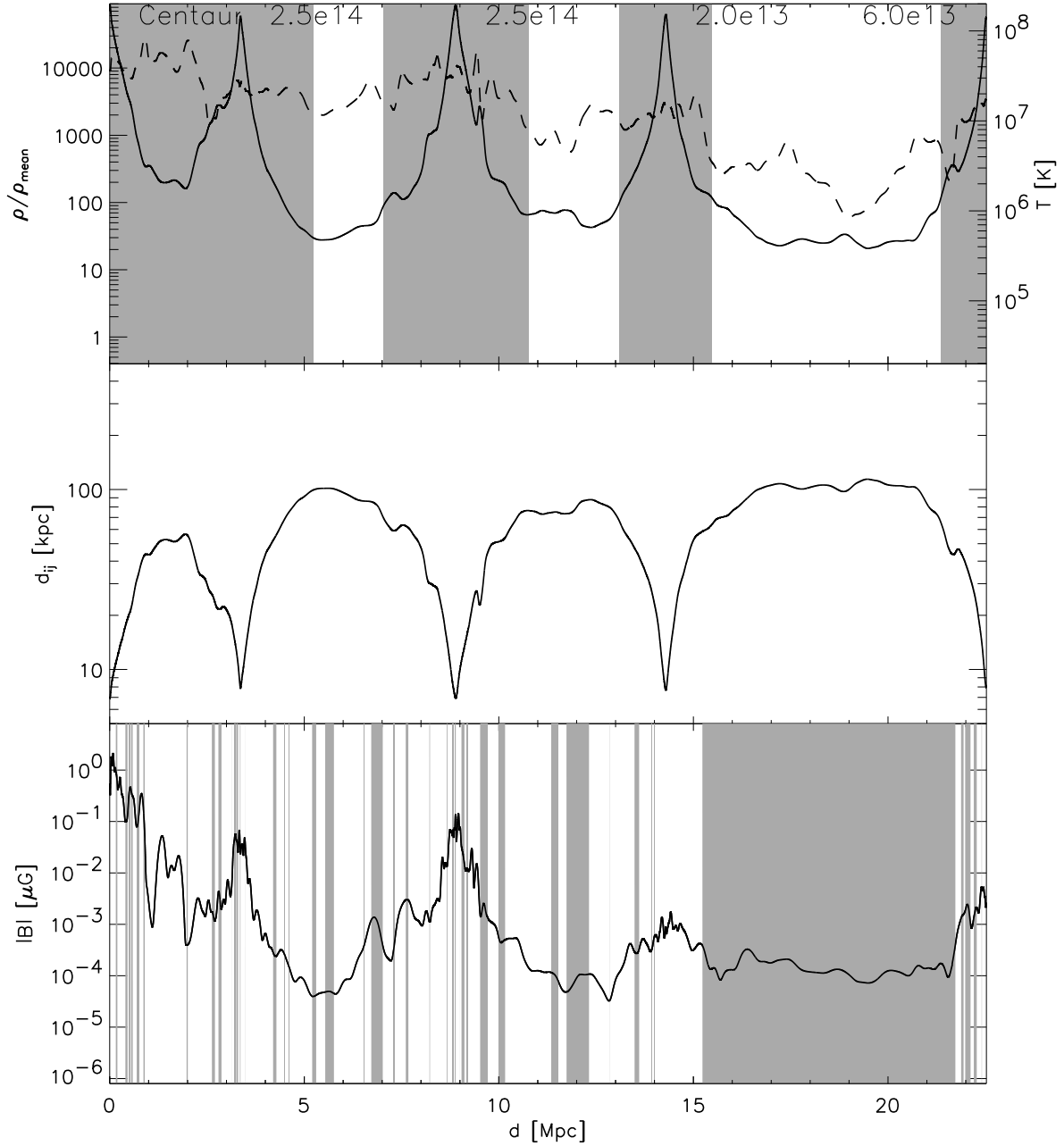


Fig. 9.— Physical state of the baryonic matter along the filamentary structure outlined in Figure 8, which starts from the Centaurus cluster and connects to several smaller halos. The panel on top shows the gas density as solid line, and the temperature as dashed line. The gray region marks the virial size of the clusters. Note that for the first two clusters, these regions overlap. The middle panel shows the mean inter-particle separation. The panel on the bottom gives the mean magnetic field strength. The gray stripes mark regions where the angle between magnetic field and the line along the filament is less than  $45^\circ$ .

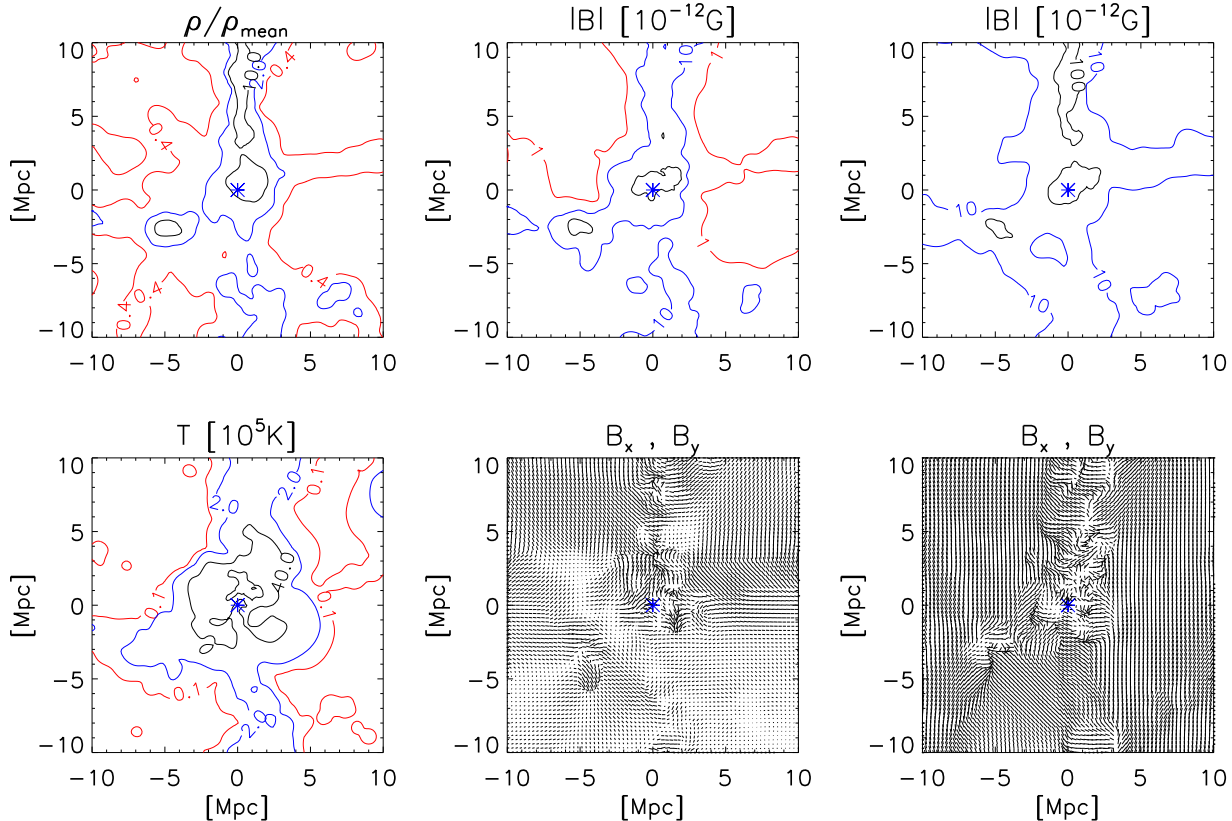


Fig. 10.— Physical state of the gas in the plane orthogonal to a filament (the plane is located in the middle of the last segment of the filamentary structure shown in Figure 9). Two panels in the left column show density and temperature contours, respectively. Panels in the middle column give the strength of the magnetic field and the direction of the normalized  $B_x$ ,  $B_y$  components for the run with the initial seed producing  $B_0 = 2 \times 10^{-12}$  G. The right column shows the same quantities, but for the run with  $B_0 = 10^{-11}$  G.

ture and is just slightly reoriented with respect to the initial field. Due to their huge extension of more than 10 Mpc and their coherent orientation of the magnetic field, sheets and voids may then also produce sizeable deflection of UHECRs, as we will discuss further in section 6

## 5.2. Magnetic fields in low-density regions

To examine the structure of MFs in low-density regions, we consider the moderate void visible within the Centaurus supercluster (see previous section). In its longest dimension this region spans over 45 Mpc and covers the space between the halos associated with the *Centaurus* cluster, *A3627*, and *Pavo*. In order to determine the state of this vast, quite underdense region, we measure physi-

cal quantities along a straight line joining the halos identified as the *Centaurus* and *Pavo* clusters. We show the results in Figure 11. In going away from the clusters, the gas density decreases continuously until, at a distance of about 10 Mpc, it reaches a value corresponding to  $\delta$  around 1, which it keeps over several tens of Mpc. While also falling towards the center of the void, the temperature shows a less well defined floor. Instead, there are signs of heating towards the outer parts of the void. This is presumably from hydrodynamic shock waves which have traveled into the cold low density regions. Because the dimension of the void orthogonal to the chosen line is smaller, such shocks may have also plausibly originated in structures ‘on the side’ of the void. The MF strength in the void follows a similar profile

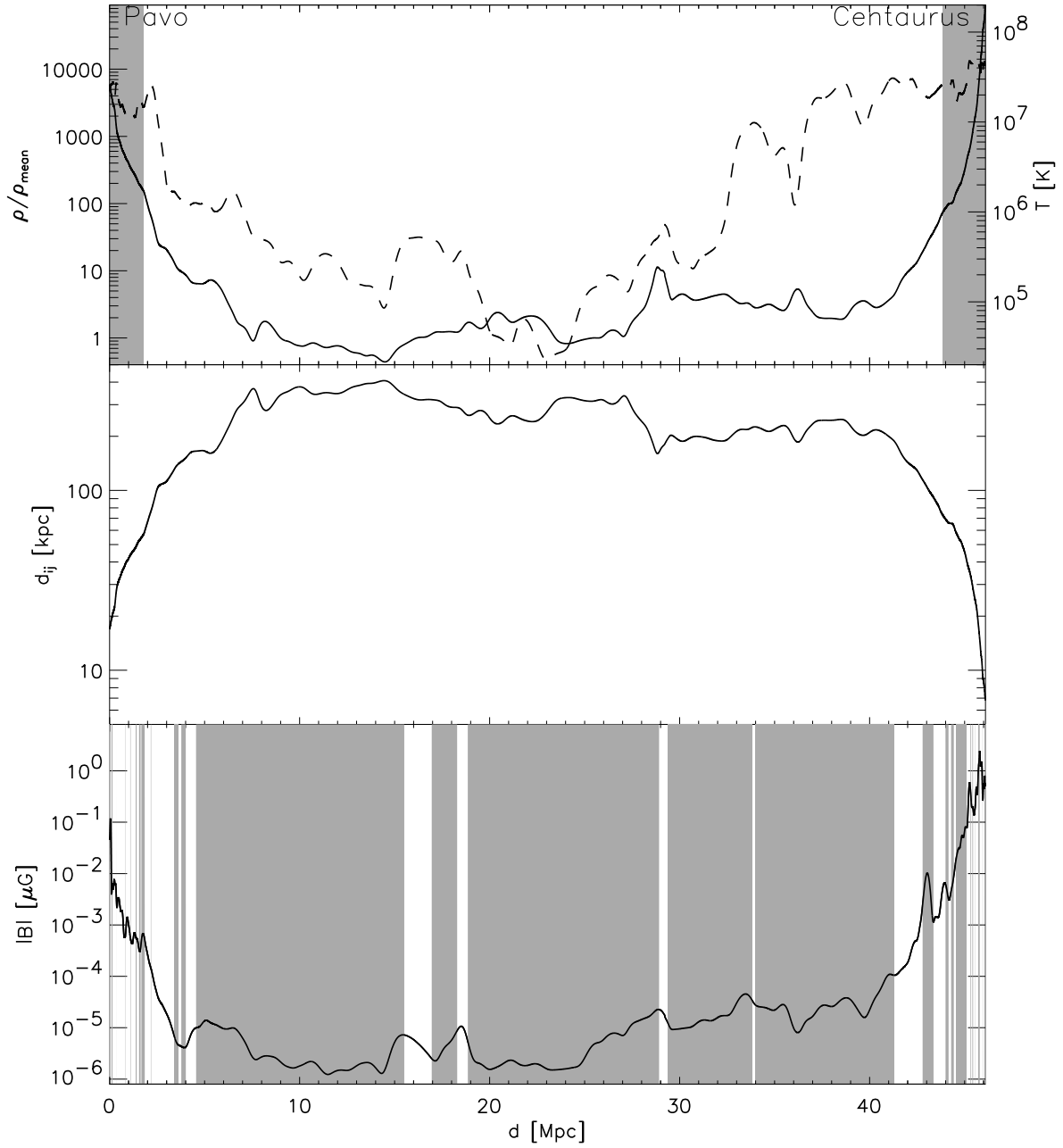


Fig. 11.— Physical state of the gas along a straight line connecting clusters A3627 and Centaurus. Note that this line-of-sight passes through a relative void within this supercluster structure (see Fig. 8). The panel on top shows the gas density as a solid line, and the temperature as a dashed line. The gray regions marks the virial size of the clusters. The middle panel gives the mean inter-particle separation of gas particles, illustrating the adaptive resolution of the simulation. The bottom panel shows the mean magnetic field strength. Here, the gray stripes mark regions where the angle between the magnetic field and the line through the void is less than  $45^\circ$ .

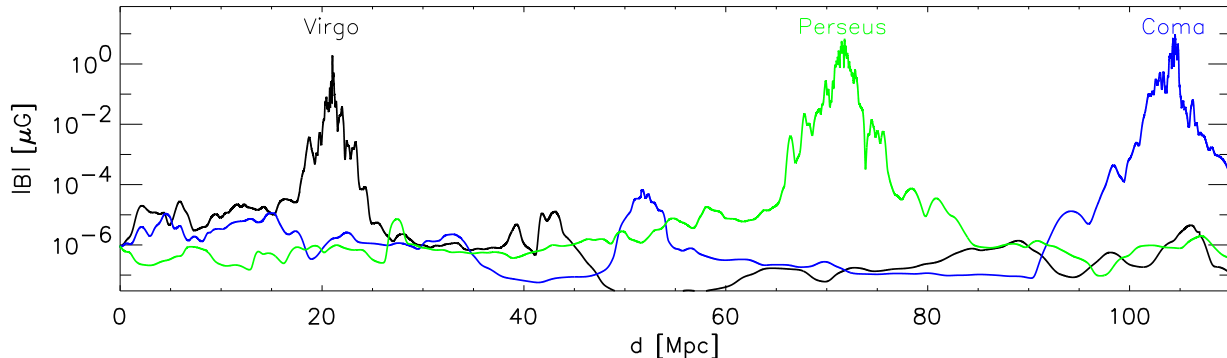


Fig. 12.— Magnetic field strength along 3 fiducial lines through the simulated volume. They are chosen to pass through the clusters Coma, Virgo (which lie within the super galactic plane) and Perseus (which is outside the super galactic plane).

as the density. Its value stays close to the comoving intensity of the seed field  $B_0$  over most of the void, retaining coherent orientation. As soon as the density grows in the proximity of the clusters, the field orientation gets randomized as a result of structure formation.

In Figure 12, we show the strength of the magnetic field along three additional lines-of-sight through our simulation, starting all from the observer position at the center (i.e. the ‘Milky Way’). The lines of sight were chosen to pass through some of the prominent clusters identified within the simulation. We selected the Coma and Virgo clusters, which lie at different angular positions in the supergalactic plane (SGP), and Perseus, which is along a line-of-sight almost perpendicular to this plane. We can see from Fig. 12 that massive clusters affect the field over substantial distances, but a few Mpc away from their cores, the field strength always drops well below  $10^{-4} \mu\text{G}$ . Apart from a region a few Mpc wide around Virgo, the field does not grow by more than an order of magnitude in the SGP, and it falls even below the comoving intensity of the seed field  $B_0$  in the direction of Perseus. The field structure is probably highly tangled in the SGP. Several big voids with  $B \ll B_0$  are also visible in the region between the border of the SGP and the Coma cluster. Similar as for filaments, the adiabatic dilution of the field in a given void can depend on the relative orientation of the magnetic seed field and the possible asymmetry in the physical expansion of the void. For an ensemble of voids in a cosmological volume,

this effect is however going to average out in the mean.

## 6. Propagation of UHE protons in the web of extra-galactic magnetic fields

A detailed knowledge of extra-galactic magnetic fields (EGMF) is particularly important for an understanding of the physics of UHECR. MFs influence the propagation of UHECR primaries. The fate of both high-energy photons<sup>6</sup> and charged nuclei depends in a crucial way on the strength and spatial structure of the EGMF.

For sufficiently small propagation distances (such that fragmentation on an infrared background is insignificant) the result for heavy nuclei can be obtained by simply multiplying proton deflections by the nucleon charge. However, the case of energetic photons is more complicated and requires dedicated study. Such an analysis is important, in particular, for a physical interpretation of correlations with BL Lacs (Tinyakov & Tkachev 2001, 2002), as seen in new independent HiRes stereo datasets which apparently require a fraction of neutral particles in UHECR (Gorbunov et al. 2004) at the level of a few percent. In this

<sup>6</sup>More precisely, MF are dumping the electromagnetic cascade initiated by HE photons, strongly limiting the propagation distance and contributing into diffuse GeV photon background, see e.g. Lee (1998); Kalashev et al. (2001). In this respect MF are important for the propagation of UHE neutrinos as well, placing important bounds on various models for the origin of UHECR (Kalashev et al. 2002).

work, however, we focus on the propagation of UHE protons in the Local Universe, leaving the case of photons and heavy nuclei for future studies.

Trajectories of charged particles in a magnetic field are bent by the Lorentz force,

$$\frac{d\vec{v}}{dt} = \frac{Ze}{E} [\vec{v} \times \vec{B}]. \quad (6)$$

Using our predicted 3D map of the magnetic field within a simulation that closely reproduces the real large-scale structure of the Local Universe, our goal is to construct an associated map of particle deflections under the action of this force.

The force, and correspondingly the resulting deflections, are inversely proportional to the particle energy  $E$ . During the course of propagation, all primaries are losing energy in interactions with various cosmic backgrounds. We have calculated accumulated deflections using two approaches. In the first approach, the energy losses are taken into account, in the second the energy appearing in Eqn. (6) is considered to be constant. The usefulness of the second approach will become clear in what follows. In both schemes, we present results as functions of energy *at the detector*, not at the source. This allows a direct physical interpretation and gives an *upper bound* on deflections. Indeed, given that  $E$  is an energy at detection, the original energy can only be larger, and true integrated deflections over the whole propagation path can only be smaller in the second scheme, where the energy losses are neglected. In the first scheme, with unknown distances to sources, we obtain an upper bound on deflections by placing all sources at the maximum distance possible.

We do not follow particle trajectories directly; instead, we compute accumulated deflections along rectilinear paths. This is a reasonable simplification, since we are not interested in actual source positions, but rather in finding “windows” where deflections are small. We cut the deflections if they exceed 5 degrees; up to this point the small angle approach we use is still a good approximation. To obtain a homogeneously sampled deflection map, we distribute sources uniformly on the sky at the maximal distance. A “whole-sky” map of deflections obtained in this way is simply a particular 2D representation of the 3D EGMF structure, and should be understood as

such. With appropriate care, such maps are ready for use in UHECR applications though.

### 6.1. Deflection maps

We considered protons with arrival energy  $E = 4 \times 10^{19}$  eV and  $E = 1 \times 10^{20}$  eV. The typical distances to sources where such primaries may originate is expected to be limited to  $\sim 500$  Mpc and  $\sim 50$  Mpc, respectively.

In the case of  $E = 1 \times 10^{20}$  eV, the process of photo-pion production in collisions with cosmic microwave background (CMB) photons,  $p + \gamma_{\text{CMB}} \rightarrow p(n) + \pi^{0(+)}$ , is the only important reaction for the energy losses (Greisen 1966; Zatsepin & Kuzmin 1966). We treat the corresponding attenuation of energy analytically in the continuous loss approximation using the expressions given in Berezhinsky & Grigor’eva (1988) and Anchordoqui et al. (1997); for a recent review see Anchordoqui et al. (2002). We distribute the sources over a sphere with radius 100 Mpc around the observer location. This propagation distance corresponds to an energy at the source of  $E_{\text{source}} \approx 1 \times 10^{22}$  eV, which we argue is a generous upper limit for the maximum acceleration energy of protons. The corresponding map of deflections is shown in the upper panel of Figure 13. Smaller values of  $E_{\text{source}}$  would correspond to smaller propagation distances, and hence smaller deflections. Larger values of  $E_{\text{source}}$  would give rise only to a minor change of the deflection map.

It is interesting to compare this map to the one obtained with energy losses being neglected; the latter is shown in Fig. 13, lower panel. Physically, given a sufficiently large set of detected events, such a map may give bounds on deflections in some rare cases when a particle travels large distances without interaction, while the former map corresponds to a statistical mean in energy losses. In other words, assuming that the underlying 3D model of EGMF is correct, the map presented in the lower panel gives a conservative upper bound on deflections diminishing the caveat of using the continuous loss approximation.

In the lower panel of Figure 14, we show the deflection map of protons with arrival energy  $E = 4 \times 10^{19}$  eV, where sources were put at a distance of 110 Mpc and energy losses were neglected. In this case, the choice of the maximal distance is

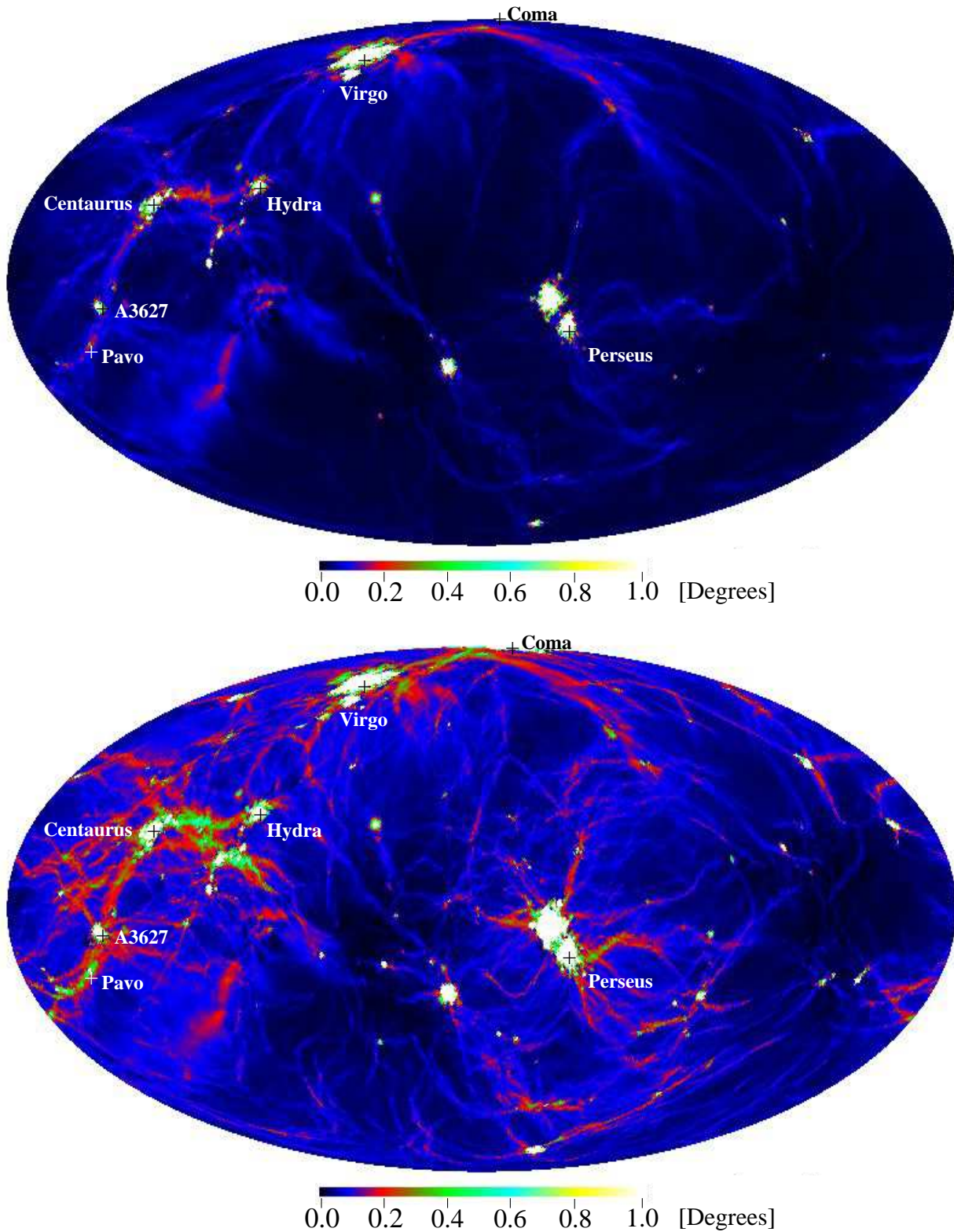


Fig. 13.— Full sky maps of expected deflection angles for protons with the arrival energy  $E = 1 \times 10^{20}$  eV. In the upper panel, energy losses have been taken into account. The coordinate system is galactic, with the galactic anti-center in the middle of the map.



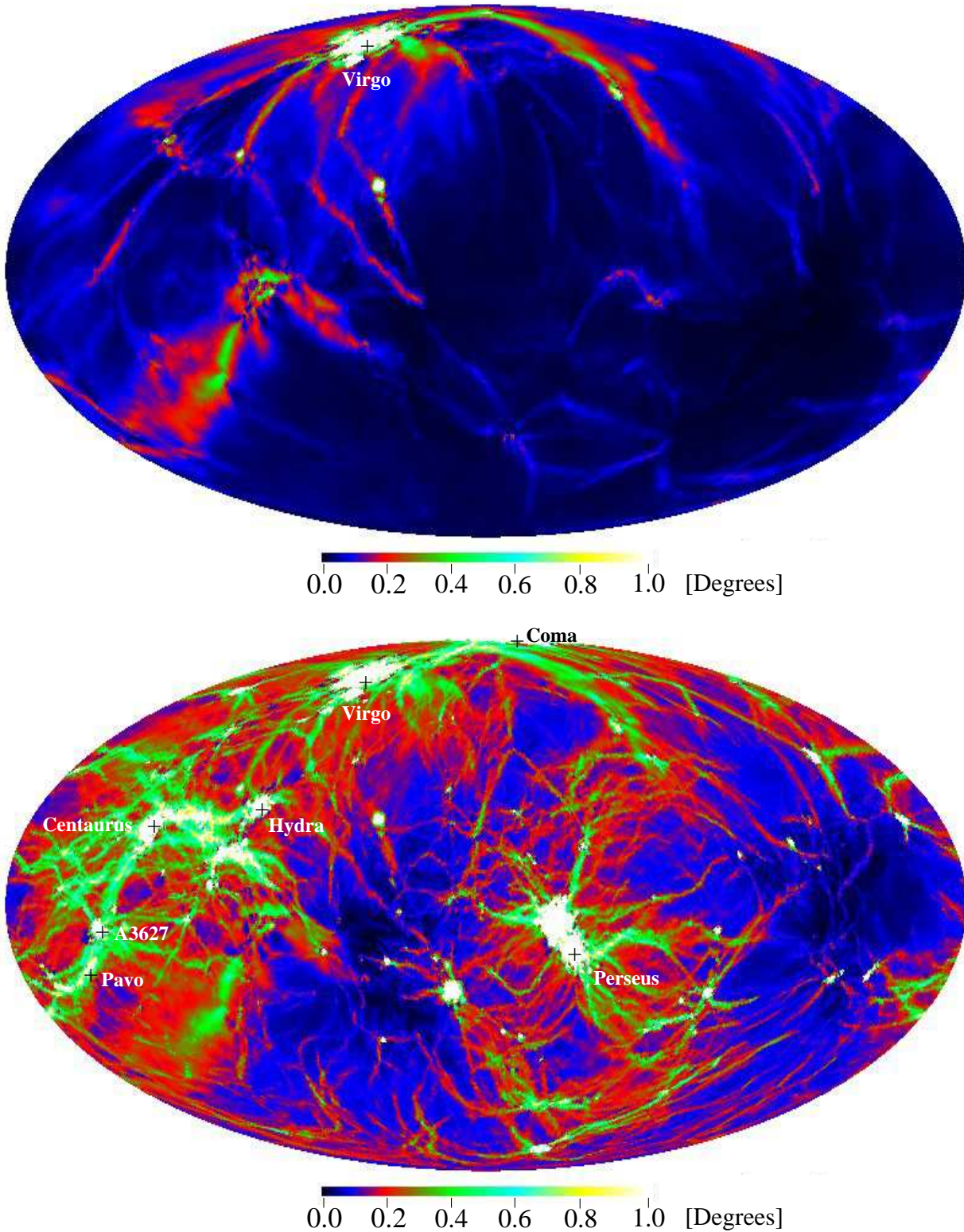


Fig. 14.— Full sky maps of expected deflection angles for protons with the arrival energy  $E = 4 \times 10^{19}$  eV. The upper panel is restricted to the 25 Mpc propagation distance, while in the lower panel the whole simulation volume within a radius of 110 Mpc around the position of the Galaxy was used.

not motivated by physical arguments, but rather by the limited size of the simulation volume. At this energy, the attenuation length is large,  $l_E \sim 1000$  Mpc (e.g. Berezhinsky et al. 2002). Therefore, the neglect of energy losses gives approximately a 10% overestimate of deflections over the distance of 110 Mpc. This effect would be nearly invisible in the map of deflections. In any case, neglecting energy losses, we obtain an upper bound for the deflections, suitable for our purposes.

Clusters and filaments imprint a clearly visible pattern in Figure 14. Large deflections are produced only when protons cross the central regions of galaxy clusters (see Rordorf et al. 2004, for a detailed study of this regime), and most of these strongest deflections are found along a strip which can be approximately identified with the Great Attractor. The observed positions of Virgo, Coma, Hydra and Centaurus lie in this region. Their locations quite precisely coincide with regions where the deflections exceed  $1^\circ$ . Perseus and other minor clusters produce large deflections in other well delineated regions of the sky. Outside clusters, which occupy only a small fraction of the sky, deflections of  $0.5^\circ$  occur along an intricate network of filaments, covering a larger area. The regions with  $\delta \ll 0.5^\circ$  correspond to voids where the MF strength is smaller than  $10^{-11}$  G.

In order to investigate the relative importance of deflectors at different distances, we also produced deflection maps that only included deflecting magnetic fields up to some maximum distance. We observe no significant deflections produced at distances smaller than 7 Mpc. The deflection map corresponding to a propagation distance of 25 Mpc from the ‘Milky Way’ is shown in Fig. 14 (upper panel). Up to this distance, only the Virgo cluster is contributing significantly. Massive clusters at large distances ( $\sim 100$  Mpc) produce large deflections but cover only a negligible fraction of the sky, so that the bulk of the deflections is produced by passages through filaments.

We note here that if a UHECR source is placed in the core of a galaxy cluster, the large deflections induced in the proton trajectory while getting out of the cluster will not result in a significant displacement, or in a smearing, of the apparent position of the source. This is because the angular size of clusters cores, barring a few nearby clusters, is smaller than the angular resolution of the UHECR

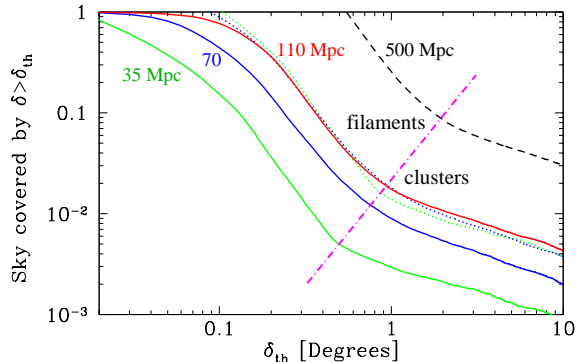


Fig. 15.— Cumulative fraction of the sky with deflection angle larger than  $\delta_{\text{th}}$ , for several values of propagation distance (solid lines). We also include an extrapolation to 500 Mpc, assuming self-similarity, based on Eqn. (7) (dashed line). To validate this scaling we show the extrapolation of  $A(\delta_{\text{th}}, d)$  from 35 Mpc and 70 Mpc to 110 Mpc (two dotted lines), giving a nice agreement with the direct calculation. The assumed UHECR energy is  $4.0 \times 10^{19}$  eV.

experiments. For this reason, even making the extreme assumption that all UHECR sources are placed in galaxy clusters would have no significant effect on the conclusions of this paper.

An additional technical argument for neglecting energy losses is that the flux of protons with  $E = 4 \times 10^{19}$  eV is expected to be dominated by sources at distances well beyond 110 Mpc, which makes extrapolation to larger distances necessary. Such an extrapolation can be obtained easily by assuming a constant energy, as described in the next subsection.

## 6.2. Extrapolation to larger distances

In Figure 15, we plot the fraction of the sky,  $A(\delta_{\text{th}})$ , over which deflections larger than  $\delta_{\text{th}}$  are found for different propagation distances, as indicated in the plot. We see that deflections larger than  $1^\circ$  are to be expected over less than 2% of the sky up to a distance of  $d = 110$  Mpc. Comparing this figure to the map of deflections, Fig. 14, we can easily identify those parts of the function  $A(\delta_{\text{th}}, d)$  which describe deflections in clusters and filaments respectively. The corresponding regions are marked in Fig. 15, and we see that the scaling



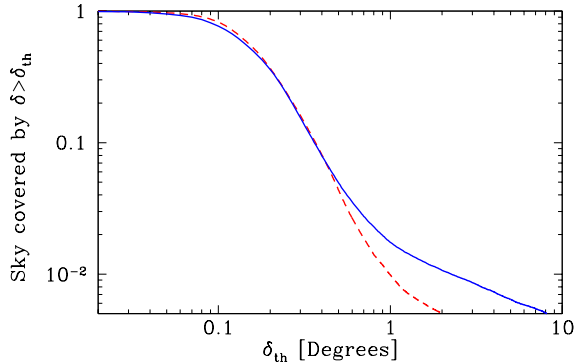


Fig. 16.— Cumulative fraction of the sky with deflection angle larger than  $\delta_{\text{th}}$ . Two runs with different MF seed are compared for  $E = 4.0 \times 10^{19}$  eV and propagation distance 110 Mpc. Results of the run with  $B_0 = 10^{-11}$  G are scaled as  $A(\delta_{\text{th}}/5, d)$  and are shown by the dashed line.

of  $A$  with  $\delta_{\text{th}}$  is different in these regions.

For large distances,  $35 < d/\text{Mpc} < 110$ , we find that  $A(\delta_{\text{th}}, d)$  approaches the self-similar behavior

$$A(\delta_{\text{th}}, d) = x^{-\beta} A(\delta_{\text{th}} \times x^\alpha, d_0), \quad (7)$$

where  $x \equiv d_0/d$ . We find that the extrapolation according to this expression is in good agreement with the direct calculation in the region of deflections dominated by multiple filament crossing ( $0.2^\circ < \delta_{\text{th}} < 1^\circ$  at  $d = 110$  Mpc) if  $\alpha = 0.5$  and  $\beta = 1$ , see Figure 15. This can be understood as follows. Self-similarity is consistent with the assumption that the density of deflectors (filaments) reaches a constant value at large distances. Since MFs are uncorrelated in different deflectors, multiple crossings should produce a “random walk” in the deflection angle, resulting in deflection angle growing as a square root of the propagation distance  $d$ , i.e. in  $\alpha = 0.5$ . On the other hand, the solid angles subtended by individual deflectors decrease as  $d^{-2}$ , while their number grows as  $d^3$ , resulting in linear growth of the total area “shadowed” by deflectors, i.e. in  $\beta = 1$ .

We use Eqn. (7) to extrapolate  $A(\delta_{\text{th}}, d)$  up to a distance of 500 Mpc. We find that even with such large distances to the sources, the expected sky coverage of deflections larger than  $1^\circ$  does not exceed 30%, see Fig. 15.

It is important to check the sensitivity of the

results to the assumed value of the seed field. We do this in Figure 16, where we compare the function  $A(\delta_{\text{th}})$  obtained for our two simulations with seed fields producing  $B_0 = 10^{-11}$  G and  $B_0 = 2 \times 10^{-12}$  G, respectively. Deflections obtained in the first run are divided by the factor of 5 and are shown by the dashed line. Both curves match each other reasonably well in the region of small deflections, but start to disagree in the region which reflect deflections in clusters. This difference with respect to a simple linear scaling should be expected, and arises due to the non-linear amplification and saturation effects.

As discussed in Section 5, the magnetic field in low density regions is affected by the coherence and the orientation of the magnetic seed field. Projected sheets that appear as filaments of low density have not undergone significant non-linear structure formation, therefore their appearance can be different for different choices of the initial field orientation. Depending on their orientation with respect to the initial field vector and the line-of-sight to the observer, the details of the filamentary structure in deflection maps differ between our two simulations which have orthogonal initial field directions. However, Figure 16 demonstrates that statistically there is no difference between the two different initial field orientations. Note also that the small filaments are unconstrained by the 1.2-Jy data imposed on the initial conditions of our simulations; instead they arise from purely random CDM fluctuations added on small scales. Finally, we remark that for a more chaotically oriented initial seed field the deflections along the filaments, sheets and voids will be accumulated as a random walk, which compared to the coherent case we have considered will tend to reduce the deflections. Again, our simulation should therefore give a robust upper limit.

Our extrapolation of cumulative deflections to distances exceeding the size of our simulation volume does not take into account the potential effect of a real unclustered component in the EGMF. This may exist in the voids and low density regions if the magnetic seed field was produced at high redshift. While the effect of such a component would not be very significant in our deflection maps because of the finite size of the simulation, it might however build up for UHECR produced at cosmological distances, and then give rise to ob-

servable deflections. Indeed, a uniform field with strength of  $2 \times 10^{-12}$  G gives rise to deflections of up to  $\approx 1^\circ$  for protons with energy  $4 \times 10^{19}$  eV, over a distance of 500 Mpc. Note however that even sizable deflections caused by the coherent field are not fatal for the identification of UHECR sources, as they can be disentangled with the use of the method suggested by Tinyakov & Tkachev (2003). Moreover, a seed field uniform over cosmological distances is unlikely. More realistically,  $l_c \ll d$  and the proton trajectory will make a random walk through the magnetic domains. The overall deflection will then be given by

$$\delta \simeq 0.2^\circ \left( \frac{B_0}{E} \frac{4 \times 10^{19} \text{ eV}}{10^{-11} \text{ G}} \right) \left( \frac{d}{1 \text{ Gpc}} \right)^{\frac{1}{2}} \left( \frac{l_c}{1 \text{ Mpc}} \right)^{\frac{1}{2}}.$$

Hence, observable deflections are not produced by the unclustered component of the IGM if  $l_c$  is smaller than a few tens of Mpc. Note that such small coherence lengths are expected from most of the proposed generation mechanisms of seed EGMFs (Grasso & Rubinstein 2001). The few mechanisms predicting larger  $l_c$  generally give rise to MF which are too weak to produce observable deflections of UHECR. Furthermore, an unclustered EGMF does not exist at all if the seed field is generated by a battery powered by structure formation (Kulsrud et al. 1997).

## 7. Conclusions and Discussion

In this work we analyzed the results of a constrained cosmological MHD simulation of the Local Universe embedded within a periodic box of  $\simeq 343$  Mpc on a side. The high resolution region centered on the ‘Milky Way’ covers a sphere with  $\simeq 115$  Mpc radius and is resolved by 50 million dark matter plus the same number of gas particles. The initial conditions were obtained using constraints from the IRAS 1.2-Jy galaxy survey complemented by a random realization of a  $\Lambda$ CDM universe. As a result, the evolved simulation at  $z = 0$  reflects the large-scale structure observed in the real Universe quite well, making it possible to identify most of the prominent halos and structures found within the simulation with known galaxy clusters and superclusters of the Local Universe. This setup removes the arbitrariness involved in choosing a suitable observer position in ordinary simulations when trying to estimate how

much the observed UHECRs may be deflected by extra-galactic magnetic fields.

We extracted the most massive clusters within the high resolution region of the simulation, leading to a set of 16 clusters (volume limited sample) within a temperature range of  $\approx 3-8$  keV. Examining the properties of the magnetic field formed in these systems, we confirm findings from earlier work. Radial profiles of the magnetic field strength are similar to that of the gas density in the outer parts, but the central magnetic field value strongly scales with the cluster temperature. During cluster formation, the magnetic seed field is not only amplified by adiabatic compression but also by shear flows that drive magnetic induction, a process that is ultimately powered by anisotropic accretion and merging events. The initial field geometry is wiped out completely by the violent cluster formation history, a result that is almost independent of the exact mechanism for generating the initial magnetic seed field, provided it is generated early enough, say before  $z \sim 3$ . This makes the strength of the comoving intensity of the seed field,  $B_0$ , essentially the only relevant free parameter of our model.

We constructed synthetic Faraday rotation measures from the simulated clusters and compared them to a variety of observational data. We demonstrated that a comoving seed field of  $B_0 = 0.2 \times 10^{-11}$  G reproduces the observed amplitude and the radial scaling of rotation measurements found in galaxy clusters very well. The strong dependence of the cluster magnetic field on cluster temperature leads to correlations between other measurable physical quantities. The predictions of our simulations for these correlations can also be confronted with observations. We demonstrated a good agreement for the scaling of the X-ray surface brightness with the rotation measure. Using two different models for the relativistic electron population, we also demonstrated that the simulated clusters are able to account for the observed correlation between radio power and temperature.

In low density regions outside of clusters, such as filaments, sheets and voids, no significant non-linear structure formation takes place and the magnetic seed field evolves mainly due to adiabatic compression. While within these regions large scale flows can still reorient the magnetic

field, it will remain correlated with the geometry of the initial seed field. The detailed structure of the field in these regions therefore depends strongly on the properties of the seed, and thereby ultimately on the mechanism which creates the seed field in the first place.

We calculated the expected deflections of ultra high energy cosmic rays by the magnetic field in the large-scale structure of the simulated Local Universe. Given that the simulation reproduces in a realistic way positions, masses and sky coverage of the prominent clusters and superclusters of the Local Universe, we have no freedom to choose the observer position. Instead, we expect that placing the observer at the position of the “Milky Way” will provide a good model for what one expects to see in the real Universe.

We have computed full sky maps of expected deflections for particles with an energy at the detector of  $4 \times 10^{19}$  eV and  $1 \times 10^{20}$  eV. These maps show that strong deflections occur only at crossing galaxy clusters. Filaments, or sheets seen in projection, can lead to some noticeable deflections, but UHECRs approaching from most areas of the sky will not suffer significant deflections by the extragalactic magnetic field. For UHECRs with arrival energies of  $1 \times 10^{20}$  eV, we also demonstrated that, if energy losses are included, the deflection will be reduced, as the traveled distance will decrease (for UHECRs with the same injection energy) and parts of the distance will be traveled at higher energies. UHECRs with energies of  $4 \times 10^{19}$  eV could in principal originate from sources up to a distance of 500 Mpc, which cannot be directly probed by our simulation. We therefore extrapolated the distribution of deflection angles for these distances, still finding that most of the sky should be covered by areas with small deflections.

Using another earlier simulation, where we chose a five times larger initial seed field that pushes the magnetic field within galaxy clusters towards (or even slightly above) the upper limit of observationally allowed magnetic field strength, we verified that even in such a more extreme model a significant fraction of the sky is covered by deflections below or comparable to the resolution of current experiments. In this second simulation we also used a different initial direction of the magnetic seed field, allowing us to explicitly verify that the statistical distribution of deflection angles is

insensitive to the direction of the initial seed field.

A major systematic uncertainty of our model is the structure of the initial magnetic seed field. However, we argue that our estimates for the typical deflection angles provide a robust upper limit. This is because an initially homogeneous magnetic seed field is expected to lead to the maximum deflection for a given field strength. Any tangled component in the seed field will reduce the deflection and therefore strengthen our final conclusion. Note also that our modeling neglects contributions to the intra-cluster magnetic field from local injection processes, related for example to galactic winds or AGNs, which probably occur also in the late phases of cluster formation. Such an additional contribution will increase the cluster magnetic field. If important and accounted for, this would then force us to lower the cosmological seed field in order to avoid exceeding the observational limits for the field in clusters. A side effect would then be a reduction of the field and of the deflection angles in low density regions, again strengthening our final conclusion.

In summary, we hence conclude that our model provides an upper limit for the expected deflections of UHE protons by the magnetic field embedded in the large-scale structure of the Local Universe. Therefore our main conclusion is that the deflections of UHE protons with energies larger than  $4 \times 10^{19}$  eV are not big enough to prevent the pointing of UHECR sources in a significant fraction of the sky. Charged particle astronomy should be possible. Note that for this purpose any deflection of the UHECRs within the primary sources or within the direct embedding environment – like for sources embedded in galaxy clusters – is irrelevant, as long as these structures are smaller than the angular resolution of the experiments, which is true even for galaxy clusters, barring the exception of a very small number of nearby clusters.

An opposite conclusion was recently reached by Sigl et al. (2004a, 2003), who on the basis of a different MHD simulation and differing physical assumptions found significant deflections of UHECRs, large enough to spoil charged particle astronomy. Their large deflections are a consequence of the much larger EGMF found in their MHD simulation, not of their different approach adopted for modeling the propagation of cosmic ray primaries. In fact, their field strength decreases more slowly

than in our simulations when going from galaxy clusters to the field, so that strong MFs extend over a larger volume and give rise to larger proton deflections. This difference can be due to several factors. Those which we were able to identify are listed below: 1) spatial resolution of the numerical codes; 2) simulation volume; 3) observer position; 4) physical assumptions about seed field.

The last issue was studied recently in Sigl et al. (2004b). It was shown that the use of cosmological seed field, as opposed to Biermann battery process with assumed subsequent turbulent amplification (which is not really well defined) does bring the result closer to ours, but cannot account for all difference.

Regarding the third issue, we note that the average MFs strength and the mean proton deflection may be significantly increased even if the observer is placed in the void but nearby a highly magnetized regions, see e.g. Fig. 1. Our simulations have clear advantage here. Using constrained simulations we remove the ambiguity in the choice of the observer position.

The first and second issues affect the result via different overall normalization of the original seed field. In both simulations the seed field is normalized to reproduce MF in the centers of clusters. If for some reason MF is undershoot in cluster centers in a given simulation, this will lead to an over-estimation of MF in filaments and voids, and vice versa.

In the simulation of Sigl et al. (2004a, 2003) the largest clusters have temperature of a few keV, corresponding to a mass significantly smaller than  $10^{15} M_{\odot}$ , while in our simulation we find clusters with temperature as large as 8 keV which is consistent with observations. Since the MF strength in the clusters is correlated with the cluster temperature (Dolag et al. 2001), the strength of ICMFs inferred from the RMs in real clusters cannot be used to normalize the MF in simulations in which the cluster population is not representative of the real one.

Numerical resolution affect our Lagrangian simulations and the Eulerian simulations of Sigl et al. (2004a, 2003) in a similar way. Since we can resolve the internal structure of galaxy clusters much better than possible with fixed mesh codes, we are confident that our normalization to the observa-

tional data on clusters is reliable. (We note that the resolution of both codes is comparable in filaments.) Note also that the analysis of the RMs of polarized radio sources observed in these systems shows that the coherence length of ICMFs is typically  $\sim 10$  kpc, comparable to the resolution we reach in clusters, but ten times smaller than the resolution reached in Sigl et al. (2004a, 2003).

It should be stressed that in our simulations the adiabatic compression and inductive amplification give roughly equal contributions into the final MF in clusters, see Fig. 7. This is a non-trivial result which has to be verified with future work.

These discrepancies highlight the significant uncertainties that still exist in predicting the structure of extragalactic magnetic fields. Clearly, more work will be required to fully resolve this issue, which is of significant relevance for the prospects of forthcoming experiments. Further progress in this will probably be driven both by refined numerical methods as well as by ever more demanding comparisons with observational data. Our present success in matching the observed correlations between the X-ray surface brightness and RMs in individual galaxy clusters, as well as the combined RMs profiles and radio halo luminosity is already highly encouraging in this respect.

## Acknowledgments

We would like to thank V.A. Berezhinsky, P. Blasi, G. Brunetti, T. Ensslin and G. Sigl for valuable discussions. The simulations were carried out at the Computing Center of the Max-Planck Society, Garching, Germany. Post-processing of the data was carried out on the IBM-SP4 machine at the ‘‘Centro Interuniversitario del Nord-Est per il Calcolo Elettronico’’ (CINECA, Bologna), with CPU time assigned under an INAF-CINECA grant. K. Dolag acknowledges support by a Marie Curie Fellowship of the European Community program ‘Human Potential’ under contract number MCFI-2001-01227.

## REFERENCES

- Anchordoqui, L., Paul, T., Reucroft, S., & Swain, J. 2003, *Int. J. Mod. Phys. A* 18, 2229 [hep-ph/0206072]
- Anchordoqui, L. A., Dova, M. T., Epele, L. N., &

- Swain, J. D. 1997, Phys. Rev., D55, 7356 [hep-ph/9704387]
- Atoyan, A. M. & Volk, H. J. 1999, astro-ph/9912557
- Ave, M., Hinton, J. A., Vazquez, R. A., Watson, A. A., & Zas, E. 2002, Phys. Rev., D65, 063007 [astro-ph/0110613]
- Bacchi, M., Feretti, L., Giovannini, G., & Govoni, F. 2003, A&A, 400, 465
- Berezinsky, V., Gazizov, A. Z., & Grigorieva, S. I. 2002, hep-ph/0204357
- Berezinsky, V. S. & Grigor'eva, S. I. 1988, Astron. Astrophys., 199, 1
- Bird, D. J. et al. 1993, Phys. Rev. Lett., 71, 3401
- Birk, G. T., Wiechen, H., & Otto, A. 1999, ApJ, 518, 177
- Blasi, P., Burles, S., & Olinto, A. V. 1999, ApJ, 514, L79
- Blasi, P. & Colafrancesco, S. 1999, Astropart. Phys., 122, 169 [astro-ph/9905122]
- Børve, S., Omang, M., & Trulsen, J. 2001, ApJ, 561, 82
- Brunetti, G. 2003, in Matter and energy in clusters of galaxies, p. 349, astro-ph/0208074.
- Brunetti, G., Setti, G., Feretti, L., & Giovannini, G. 2001, MNRAS, 320, 365
- Bruni, M., Maartens, R., & Tsagas, C. G. 2003, MNRAS, 338, 785
- Carilli, C. L. & Taylor, G. B. 2002, ARA&A, 40, 319
- Clarke, T. E., Kronberg, P. P., & Böhringer, H. 2001, ApJ, 547, L111
- Dolag, K., Bartelmann, M., & Lesch, H. 1999, A&A, 348, 351
- Dolag, K., Bartelmann, M., & Lesch, H. 2002, A&A, 387, 383 [astro-ph/0202272]
- Dolag, K. & Enßlin, T. A. 2000, A&A, 362, 151
- Dolag, K., Grasso, D., Springel, V., & Tkachev, I. 2003, in *28th International Cosmic Ray Conference (ICRC 2003)*, Tsukuba, Japan, Vol. 1, 735 [astro-ph/0308155]
- Dolag, K., Grasso, D., Springel, V., & Tkachev, I. 2004, JETP Lett., 79, 583 [astro-ph/0310902]
- Dolag, K., Schindler, S., Govoni, F., & Feretti, L. 2001, A&A, 378, 777
- Enßlin, T. A. 2002, in IAU Symposium, p. 141
- Enßlin, T. A., Lieu, R., & Biermann, P. L. 1999, A&A, 344, 409
- Enßlin, T. A. & Vogt, C. 2003, A&A, 401, 835
- Feretti, L. 1999, in Diffuse Thermal and Relativistic Plasma in Galaxy Clusters, p. 3
- Feretti, L., Dallacasa, D., Giovannini, G., & Tagliani, A. 1995, A&A, 302, 680
- Feretti, L., Dallacasa, D., Govoni, F., et al. 1999a, A&A, 344, 472
- Feretti, L., Perley, R., Giovannini, G., & Andernach, H. 1999b, A&A, 341, 29
- Furlanetto, S. R. & Loeb, A. 2001, ApJ, 556, 619
- Fusco-Femiano, R., dal Fiume, D., Feretti, L., et al. 1999, ApJ, 513, L21
- Fusco-Femiano, R., Orlandini, M., Brunetti, G., et al. 2004, ApJ, 602, L73
- Giovannini, G., Feretti, L., Venturi, T., Kim, K.-T., & Kronberg, P. P. 1993, ApJ, 406, 399
- Gorbunov, D. S., Tinyakov, P. G., Tkachev, I. I., & Troitsky, S. V. 2004, JETP Lett., 80, 145 [astro-ph/0406654]
- Govoni, F., Enßlin, T. A., Feretti, L., & Giovannini, G. 2001, A&A, 369, 441
- Grasso, D. & Rubinstein, H. R. 2001, Phys. Rept., 348, 163 [astro-ph/0009061]
- Greisen, K. 1966, Phys. Rev. Lett., 16, 748
- Hoffman, Y. & Ribak, E. 1991, ApJ, 380, L5
- Kalashov, O. E., Kuzmin, V. A., Semikoz, D. V., & Sigl, G. 2002, Phys. Rev., D66, 063004 [hep-ph/0205050]

- Kalashv, O. E., Kuzmin, V. A., Semikoz, D. V., & Tkachev, I. I. 2001, astro-ph/0107130
- Kim, K.-T., Kronberg, P. P., & Tribble, P. C. 1991, ApJ, 379, 80
- Kronberg, P. P., Lesch, H., & Hopp, U. 1999, ApJ, 511, 56
- Kulsrud, R. M., Cen, R., Ostriker, J. P., & Ryu, D. 1997, ApJ, 480, 481 [astro-ph/9607141]
- Lee, S. 1998, Phys. Rev., D58, 043004 [astro-ph/9604098]
- Liang, H., Hunstead, R. W., Birkinshaw, M., & Andreani, P. 2000, ApJ, 544, 686
- Mathis, H., Lemson, G., Springel, V., et al. 2002, MNRAS, 333, 739 [astro-ph/0111099]
- Murgia, M. et al. 2004, astro-ph/0406225
- Rephaeli, Y., Gruber, D., & Blanco, P. 1999, ApJ, 511, L21
- Roettiger, K., Stone, J. M., & Burns, J. O. 1999, ApJ, 518, 594
- Rordorf, C., Grasso, D., & Dolag, K. 2004, astro-ph/0405046
- Rossetti, M. & Molendi, S. 2004, A&A, 414, L41
- Ryu, D., Kang, H., & Biermann, P. L. 1998, A&A, 335, 19
- Sarazin, C. L. 2002, The Physics of Cluster Mergers (ASSL Vol. 272: Merging Processes in Galaxy Clusters), p. 1
- Shinozaki, K. et al. 2003, in 28th International Cosmic Ray Conference (ICRC 2003), Tsukuba, Japan, Vol. 1, p. 401
- Sigl, G., Miniati, F., & Ensslin, T. 2003, Phys. Rev., D68, 043002 [astro-ph/0302388]
- Sigl, G., Miniati, F., & Ensslin, T. 2004a, astro-ph/0401084
- Sigl, G., Miniati, F., & Ensslin, T. 2004b, astro-ph/0409098
- Springel, V. & Hernquist, L. 2002, MNRAS, 333, 649
- Springel, V., Yoshida, N., & White, S. 2001, New Astronomy, 6, 79
- Taylor, G. B., Govoni, F., Allen, S. A., & Fabian, A. C. 2001, Mon. Not. Roy. Astron. Soc., 326, 2 [astro-ph/0104223]
- Tinyakov, P. & Tkachev, I. 2003, in 28th International Cosmic Ray Conference (ICRC 2003), Tsukuba, Japan, Vol. 1, 671 [astro-ph/0305363]
- Tinyakov, P. G. & Tkachev, I. I. 2001, JETP Lett., 74, 445 [astro-ph/0102476]
- Tinyakov, P. G. & Tkachev, I. I. 2002, Astropart. Phys., 18, 165 [astro-ph/0111305]
- Völk, H. J. & Atoyan, A. M. 2000, ApJ, 541, 88
- Venturi, T., Bardelli, S., Dallacasa, D., et al. 2003, A&A, 402, 913
- Vogt, C. & Enßlin, T. A. 2003, A&A, 412, 373
- Zatsepin, G. T. & Kuzmin, V. A. 1966, JETP Lett., 4, 78

---

This 2-column preprint was prepared with the AAS L<sup>A</sup>T<sub>E</sub>X macros v5.0.